Subgrid-scale effects in compressible variable-density decaying turbulence

Sidharth GS¹† and Graham V. Candler¹

 $^1\mathrm{Aerospace}$ Engineering and Mechanics, University of Minnesota, Minneapolis, MN 55414, USA

(Received xx; revised xx; accepted xx)

Many turbulent flows are characterized by complex scale interactions and vorticity generation caused by compressibility and variable-density effects. In the large-eddy simulation of variable-density flows, these processes manifest themselves as subgrid-scale (SGS) terms that interact with the resolved-scale flow. This paper studies the effect of the variable-density SGS terms and quantifies their relative importance. We consider the SGS terms appearing in the density-weighted Favre-filtered equations and in the unweighted Reynolds-filtered equations. The conventional form of the Reynolds-filtered momentum equation is complicated by a temporal SGS term; therefore, we derive a new form of Reynolds-filtered governing equations that does not contain this term and has only double correlation SGS terms. The new form of the filtered equations has terms that represent the SGS mass flux, pressure-gradient acceleration, and velocity-dilatation correlation. To evaluate the dynamical significance of the variable-density SGS effects, we carry out direct numerical simulations of compressible decaying turbulence at a turbulent Mach number of 0.3. Two different initial thermodynamic conditions are investigated: homentropic, and a thermally inhomogeneous gas with regions of differing densities. The simulated flow fields are explicitly filtered to evaluate the SGS terms. The importance of the variabledensity SGS terms is quantified relative to the SGS specific stress, which is the only SGS term active in incompressible constant-density turbulence. It is found that while the variable-density SGS terms in the homentropic case are negligible, they are dynamically significant in the thermally inhomogeneous flows. Investigation of the variable-density SGS terms is therefore important, not only for developing variable-density closures, but also to improve the understanding of scale interactions in variable-density flows.

1. Introduction

Variable-density flows are ubiquitous in technology and nature. For example, significant variations in fluid density are encountered in high-speed flight, combustion, multi-phase flows and inertial confinement fusion. In nature, atmospheric and oceanic convection as well as astrophysical phenomena involve variable-density fluid dynamics.

Density variations in fluids can have different physical origins such as compressibility, thermal, compositional and phase inhomogeneity, chemical reactions and external energy sources and sinks. Primarily, there are two ways in which variations in the local density field interact with the local velocity field (Lele 1994): inertial effects, in which spatial variations in density correspond to spatial variations in the local pressure-gradient driven acceleration field, and dilatational effects, in which the Lagrangian variation in density corresponds to compression or expansion of the local Eulerian fluid element. These local interactions can significantly alter global flow dynamics. An important example of inertial

effects is the case of variable density jets, where the jet to free-stream density ratio affects the global stability characteristics (Sreenivasan et al. 1989; Monkewitz et al. 1990), in free and transverse jets (Getsinger et al. 2012). Another example of an inertial effect is the case of interfacial instabilities associated with accelerated variable-density interfaces, such as Rayleigh-Taylor (Joly et al. 2005) and Richtmyer-Meshkov instabilities (Brouillette 2002). The primary mechanism underlying these instabilities is baroclinic torque. The torque is produced by misalignment of independent thermodynamic quantities like pressure and density or equivalently, temperature and entropy, and is represented in the general form of the vorticity equation.

$$\frac{\partial \vec{\omega}}{\partial t} + \nabla \times (\vec{\omega} \times \vec{v}) = \frac{1}{\rho^2} \nabla \rho \times \nabla p + \nabla \times \left(\frac{\nabla \cdot \sigma}{\rho}\right) + \nabla \times \vec{F}^b$$
 (1.1)

where the σ_{ij} is the viscous stress tensor and \vec{F}^b is non-conservative body force. In the framework of the Kovasznay decomposition of turbulent fluctuations (Kovasznay 1953), the interaction of acoustic and entropy modes produces vorticity modes via the baroclinic source term. This torque is also the primary vorticity source in shock-bubble (Ranjan et al. 2011) and shock-flame interactions (Thomas et al. 2001). Baroclinic instability and associated turbulence is also observed in the form of mid-latitude storms in the atmosphere (Pierrehumbert & Swanson 1995) and mesoscale eddies in the ocean (Gill et al. 1974). In the atmosphere, earth's rotation and differential heating produce vorticity, while in the oceans, horizontal density gradients are responsible. Secondary instabilities due to baroclinic torque are observed in two-dimensional Kelvin-Helmoltz billows of variable-density shear layers, as shown in the work of Fontane & Joly (2008); Reinaud et al. (2000). Variable-density inertial effects are not only restricted to instabilities in quiescent flow states, but are also present in fully turbulent flows. For example, the density ratio of the streams in a mixing layer affects the entrainment ratio and composition of molecularly-mixed fluid in mixing layers (Miller et al. 1998; Frieler & Dimotakis 1988). This is in addition to the reduction in growth rate and structural changes associated with increasing compressibility (Brown & Roshko 1974; Pantano & Sarkar 2002; Vreman et al. 1996; Freund et al. 2000; Ferrer et al. 2017) and/or combustion-induced heat release. The composition of molecularly-mixed fluid has direct implications in the case of reactive mixing. In the reacting case, dilatational and baroclinic effects associated with heat release also contribute to the vorticity dynamics. Similarly, high-speed turbulent boundary layers exhibit significant variable-density effects due to near-wall thermal gradients (Spina et al. 1994). This is reflected in the inertial transformations used to collapse the velocity profiles, such as the mean-density-based Van Driest transformation for adiabatic boundary layers (Van Driest 1951) and meandensity-gradient-based transformations for non-adiabatic walls (Patel et al. 2016; Trettel & Larsson 2016).

Simulations of technologically-relevant variable-density turbulent flows require truncation of the spatio-temporal scales of the computed physical fields due to computational expense. Exclusion of information that represents a part of the physical system introduces the closure problem via the non-linearity of the governing equations. For accurate simulations, the closure problem has to be addressed, whether the simulations compute the time-averaged fields as in Reynolds averaged Navier-Stokes (RANS) or the spatially filtered fields, as in large eddy simulations (LES). This paper focuses on the closure problem that results from non-representation of small-scale density fluctuations in large eddy simulations. The set of terms that require closure depends on the choice of the computed velocity field. For example, in the context of RANS, the choice of computed

velocity variable can be either the time-averaged velocity or the density-weighted time-averaged velocity. The density-weighted averaging concept, also known as Favre averaging (Favre 1969) is predominantly used. This method does not require closure of the mass conservation equation and retains the mathematical structure of the unclosed terms in a form that is structurally similar to their constant-density counterparts. Likewise, in LES, the resolved-scale velocity may be represented by the filtered velocity or Favre-filtered velocity. With the exception of the work of Yoshizawa (1986); Boersma & Lele (1999) and Sun & Lu (2006), the Favre-filtered velocity is almost exclusively employed. The two velocity fields represent two different physical variables and their evolution is governed by different dynamics. An analogy may be drawn between the two resolved-scale velocities and the concept of mass velocity and momentum velocity introduced as bi-velocity hydrodynamics in Brenner (2009).

Favre (1992) cites the importance of mass-averaged velocity for statistical analysis by stating that "the mean stream-surfaces lose their physical meaning as the mean stream-surfaces are crossed by the mean mass flux" in the case of Reynolds-averaged velocity. It is important to consider Favre's statement in the context of RANS and LES. While in RANS, steady-state stream surfaces would be desirable for the description of the flow-state, but this may not hold true for LES filter volumes. The resolved-scale velocity represents the local value of the filtered Eulerian velocity field, and may not necessarily represent the velocity of a frame of reference in which there is net zero SGS mass diffusion through the LES filter volume. Therefore, in this paper, in addition to the Favre-filtered velocity formulation, we also consider unclosed terms arising in filteredvelocity based equations, which we refer to as the Reynolds-filtered formulation. We also note that the resolved-scale thermodynamic variables may be represented identically, Reynolds-filtered or Favre-filtered, irrespective of the choice of resolved-scale velocity. This is important as the representation of resolved-scale thermodynamic quantities is required to be consistent with the laws of thermodynamics (Favre 1992; Chassaing 1997). From the point of resolved-scale vorticity statistics, the Reynolds-filtered velocity is the preferred variable. This is because the curl of the Favre-filtered velocity does not mathematically equal the Favre-filtered vorticity. This holds more generally for the resolved-scale velocity gradient tensor. Representation of resolved-scale vorticity by a compound variable involving the density field can have implications during subgrid-scale (SGS) modeling where information from small velocity scales, close to the filter width primarily guides the closure. In some previous work that use the Favre-filtered velocity formulation, the filtered velocity is algebraically estimated for closure even though it is not transported. This is discussed within an eddy viscosity framework in Germano (1996); Germano et al. (2014), and within the stretched-vortex model in Sidharth et al. (2014). However, the equations based on Reynolds-filtered velocity are not commonly used because they require closure of additional SGS terms in the momentum equation. This includes an unsteady time-derivative term that can, in the case of strong density variations, be more significant than the SGS stress term (Chesnel et al. 2011). In the present work, we will address this issue by deriving a new set of equations based on Reynolds-filtered velocity, and that has a closure set with SGS terms that depend on double correlations. Although the equations are developed for LES, they are applicable to RANS due to the formal equivalence.

A review of the progress made in variable-density turbulence modeling is relevant as it helps identify unclosed terms that are important in these classes of flows. Since spatio-temporal variations in fluid density can have different physical origins, a variety of modeling techniques exist, spanning low-speed variable-density turbulent mixing to the high-speed turbulent flows and combustion. RANS modeling for variable-density

turbulence has been a research field for several decades. Chassaing (2001) and Chassaing et al. (2013) provide a comprehensive review of variable-density modeling in RANS closure schemes. In first-order closures, variable-density effects in the $k-\epsilon$ framework have been extensively studied. Important variable-density terms investigated are the turbulent mass flux (Ristorcelli 1993), the pressure-dilatation (Sarkar 1992), and the dilatational dissipation (Zeman 1990). Also, terms associated with baroclinic torque and compression in the solenoidal dissipation rate equation have received interest (Sinha & Candler 2003; Kreuzinger et al. 2006). Some modeling techniques estimate the variance of density (Taulbee & VanOsdol 1991; Banerjee et al. 2010) and pressure (Zeman 1991). Within second-order closures, density fluctuation correlations have been analyzed in the work of Shih et al. (1987); Chassaing et al. (1994); Yoshizawa et al. (2013) and Schwarzkopf et al. (2011). Pressure-strain (Adumitroaie et al. 1999) and pressure-acceleration-massflux terms (Lindstedt & Vaos 1999) have been shown to be important for closure in second-order moment equations. It is important to note that in both first-order and second-order modeling, the Favre-averaged velocity is usually the solution variable. Shih et al. (1987) investigate the evolution of non-density-averaged velocity in a variabledensity mixing layer, but use constant-density approximation for the turbulent pressureacceleration term appearing in the equation for mean velocity. In the class of algebraic second-order closures, an explicit algebraic stress model for compressible variable-density turbulent flows has been proposed (Grigoriev et al. 2015), where the effect of densityvelocity correlations on turbulence is accounted for. The authors in this work state their preference of Reynolds averaging over Favre averaging due to turbulent dissipation being a function of the fluctuating velocity field, and not the density-averaged fluctuating velocity. Similarly, in the class of stochastic methods for turbulent flow simulation, variable-density effects such as differential acceleration have been included in the work of Bakosi & Ristorcelli (2011).

A significant effort to understand variable-density and dilatational effects in turbulence has been carried out for turbulent premixed flames (Sabelnikov & Lipatnikov 2017; Lipatnikov & Chomiak 2010; Robin et al. 2011). For example, Libby & Bray (1977) have pointed out that modeling of variable-density effects in turbulent flames is important and that there can be large differences between the Favre-averaged and the Reynoldsaveraged scalars and velocities in the flame zone. Also, assumptions such neglecting third-order covariances can lead to inconsistent results. They also find that the Favreaveraged turbulent kinetic energy production due to the pressure-acceleration-mass-flux term can override the suppression due to dilatation and cause counter-gradient turbulent diffusion of scalar concentration (Bray et al. 1981; Libby & Bray 1981; Bilger 1976). The authors state that their results "constitute a warning as to the dangers of carrying over the empiricism developed in constant-density flows to variable density flows in general and to turbulent reacting flows with significant heat release in particular." Countergradient diffusion of scalars is more generally a variable-density effect in turbulence and has also been observed in inert helium-air mixing (LaRue & Libby 1977). Variabledensity effects in turbulent flames have also been discussed extensively in Chomiak & Nisbet (1995). It must be noted however that the major focus of RANS analysis has been restricted to variable-density effects on the transport of second-order turbulent quantities. With regard to LES, there have been efforts to understand the role of filtered velocity and Favre-filtered velocity in turbulent flame dynamics. Chakraborty et al. (2017) show that the difference between the orientation of the vorticity vector obtained from the filtered velocity and Favre-filtered velocity in planar turbulent flames can be large. Serra et al. (2014) account for the difference between the Favre-filtered scalar and the filtered scalar using the SGS specific volume flux, similar to the approach presented in Sidharth

et al. (2014). The concept of counter-gradient diffusion due to variable-density effects is observed in LES as well, but with different physical connotations (Klein et al. 2015).

We focus on the variable-density SGS terms that appear in the resolved-scale momentum equation as opposed to terms that appear in the transport equations of SGS terms. The terms under consideration are listed in Section 2 where we review the filtered compressible Navier-Stokes equations in the Favre-filtered and the Reynolds-filtered formulations. A new form of Reynolds-filtered governing equations is derived using the transport equations of SGS mass flux and SGS kinetic energy. This form of the governing equations does not contain unsteady unclosed terms. Flow fields from direct numerical simulations of single-fluid decaying isotropic turbulence with dynamically significant dilatational and inertial variable-density effects are used for the explicit evaluation of the SGS terms. The setup of the direct numerical simulations and results from the SGS analysis are discussed in Sections 3 and 4.

2. Filtered Navier-Stokes equations

Let us first review the formalism for filtering the Navier-Stokes equations and revisit the resulting governing equations. A spatio-temporal linear filter for a flow-realization with $\mathbf{x} = x_i$ may be defined as

$$\overline{f(\mathbf{x},t)} = \int G_{\Delta_x,\Delta_t}(\mathbf{x} - \mathbf{x}', t - t') f(\mathbf{x}', t) d^3 \mathbf{x}' dt'$$
(2.1)

where G_{Δ_x,Δ_t} is the convolution kernel with an associated filter length scale Δ_x and a filter time scale Δ_t , satisfying

$$\int G_{\Delta_x,\Delta_t}(\mathbf{x} - \mathbf{x}')d^3\mathbf{x}'dt' = 1$$
(2.2)

For large eddy simulation, filters are spatial and no temporal filtering is considered in this paper. It must be noted that the continuous filter is independent of the filter associated with the discrete solution field and the discrete differential operators used for numerical computation. We assume that the continuous filter is homogeneous and therefore commutes with the continuous differential operator. The governing equations for filtered mass, momentum, and energy are obtained from the filtered Navier-Stokes equations.

$$\frac{\partial}{\partial t} \begin{pmatrix} \bar{\rho} \\ \bar{\rho}u_i \\ \frac{1}{2} \overline{\rho u_k u_k} + \bar{E}_{int} \end{pmatrix} + \frac{\partial}{\partial x_j} \begin{pmatrix} \overline{\rho u_j} \\ \overline{\rho u_i u_j} + \bar{p}\delta_{ij} \\ \frac{1}{2} \overline{\rho u_k u_k} + \overline{E}_{int} u_j + \overline{p}u_j \end{pmatrix} = \begin{pmatrix} 0 \\ \bar{\sigma}_{\rho u_i} \\ \bar{\sigma}_E \end{pmatrix}$$
(2.3)

 $E_{\rm int}$ represents the internal energy per unit volume. The terms $\sigma_{\rho u_i}$ and σ_E correspond to diffusive molecular transport in the momentum and the energy equations, respectively. In the present analysis, the resolved-scale and the SGS terms that arise from the expressions from $\bar{\sigma}_{\rho u_i}$ and $\bar{\sigma}_E$ are not expanded.

2.1. Favre-filtered velocity formulation

In the Favre-filtered velocity formulation, the filtered Navier-Stokes equations for variable-density flows are written in a form that uses the density-weighted filtered velocity as the resolved-scale velocity.

$$\frac{\partial}{\partial t} \begin{pmatrix} \bar{\rho} \\ \bar{\rho}\tilde{u}_{i} \\ \bar{E}_{\text{int}} + \frac{1}{2}\bar{\rho}\tilde{u}_{k}\tilde{u}_{k} + \frac{1}{2}\tau_{kk}^{\text{F}} \end{pmatrix} + \frac{\partial}{\partial x_{j}} \begin{pmatrix} \bar{\rho}\tilde{u}_{j} \\ \bar{\rho}\tilde{u}_{i}\tilde{u}_{j} + \bar{p}\delta_{ij} \\ \frac{1}{2}\bar{\rho}\tilde{u}_{k}\tilde{u}_{k}\tilde{u}_{j} + \bar{E}_{\text{int}}\tilde{u}_{j} + \bar{p}\tilde{u}_{j} \end{pmatrix} + \frac{\partial}{\partial x_{j}} \begin{pmatrix} 0 \\ \tau_{ij}^{\text{F}} \\ \mathcal{K}_{j}^{\text{F}} + \mathcal{H}_{j}^{\text{F}} \end{pmatrix} = \begin{pmatrix} 0 \\ \bar{\sigma}_{\rho u_{i}} \\ \bar{\sigma}_{E} \end{pmatrix}$$
(2.4)

A Favre-filtered quantity is denoted by

$$\tilde{f} = \frac{\overline{\rho f}}{\bar{\rho}} \tag{2.5}$$

The resolved-scale velocity, \tilde{u}_i , is therefore obtained from the filtered momentum and the filtered density. The SGS terms in this formulation are the SGS stress tensor $\tau_{ij}^{\rm F}$, the SGS kinetic energy flux, $\mathcal{K}_{j}^{\rm F}$ and the SGS enthalpy flux $\mathcal{H}_{j}^{\rm F}$.

$$\tau_{ij}^{\mathrm{F}} = \overline{\rho u_i u_j} - \bar{\rho} \tilde{u}_i \tilde{u}_j, \ \mathcal{K}_j^{\mathrm{F}} = \overline{\rho u_k u_k u_j} - \bar{\rho} \tilde{u}_k \tilde{u}_k \tilde{u}_j, \ \mathcal{H}_j^{\mathrm{F}} = \overline{(E_{\mathrm{int}} + p) u_j} - (\bar{E}_{\mathrm{int}} + \bar{p}) \tilde{u}_j \ (2.6)$$

The filtered convective stress $\overline{\rho u_i u_j}$ is equivalent to the Favre-filtered specific stress $\bar{\rho} u_i u_j$. The expression for the SGS stress $\tau_{ij}^{\rm F} = \bar{\rho} (\widetilde{u_i u_j} - \tilde{u}_i \tilde{u}_j)$ appears as a variable-density analog of the constant-density specific stress tensor $\overline{u_i u_j} - \bar{u}_i \bar{u}_j$.

The variable-density SGS contribution to the momentum equation can be written explicitly if we represent the SGS terms using central moments (Germano 1992). Let us denote the central moments under the filter operator as

$$\mathcal{T}\left[a,b\right] = \overline{ab} - \bar{a}\bar{b} \tag{2.7}$$

$$\mathcal{T}[a,b,c] = \overline{abc} - \bar{a}\mathcal{T}[b,c] - \bar{b}\mathcal{T}[a,c] - \bar{c}\mathcal{T}[a,b] - \bar{a}\bar{b}\bar{c}$$
(2.8)

where a, b, c are field variables. The SGS stress tensor can then be expressed as

$$\tau_{ij}^{F} = \bar{\rho}(\widetilde{u_i u_j} - \tilde{u}_i \tilde{u}_j) = \bar{\rho} \mathcal{T}[u_i, u_j] + \mathcal{T}[\rho, u_i, u_j] - \frac{1}{\bar{\rho}} \mathcal{T}[\rho, u_i] \mathcal{T}[\rho, u_j]$$
 (2.9)

Equation 2.9 (Germano et al. 2014) shows that the SGS stress tensor in either formulation involves three unclosed terms: the SGS specific stress tensor $\mathcal{T}[u_i, u_j]$, the SGS mass flux $\mathcal{M}_i = \mathcal{T}[\rho, u_i]$, and the SGS trivariate moment $\mathcal{T}[\rho, u_i, u_j]$. Although absent in the mass conservation equation, the SGS mass flux \mathcal{M}_i affects the Favre-filtered velocity SGS stress τ_{ij}^{F} . The SGS trivariate moment also appears when momentum $\mathfrak{p}_i = \rho u_i$ is used as the variable of interest.

$$\tau_{ij}^{F} = \mathcal{T}\left[\mathfrak{p}_{i}, \mathfrak{p}_{j}, \frac{1}{\rho}\right] + \frac{\overline{1}}{\rho} \mathcal{T}\left[\mathfrak{p}_{i}, \mathfrak{p}_{j}\right] + \bar{\mathfrak{p}}_{i} \mathcal{T}\left[\mathfrak{p}_{j}, \frac{1}{\rho}\right] + \bar{\mathfrak{p}}_{j} \mathcal{T}\left[\mathfrak{p}_{i}, \frac{1}{\rho}\right] - \frac{\bar{\mathfrak{p}}_{i}\bar{\mathfrak{p}}_{j}}{\bar{\rho}} \mathcal{T}\left[\rho, \frac{1}{\rho}\right]$$
(2.10)

Similarly, the SGS term \mathcal{K}_{j}^{F} appearing in the filtered total energy equation can be shown to consist of a fourth-order moment SGS term.

2.2. Reynolds-filtered velocity formulation

Now, let us represent the filtered Navier-Stokes equations using the filtered velocity.

In this formulation, the equations are

$$\frac{\partial}{\partial t} \begin{pmatrix} \bar{\rho} \\ \bar{\rho} \bar{u}_{i} + \mathcal{M}_{i} \\ \bar{E}_{\text{int}} + \frac{1}{2} \bar{\rho} \bar{u}_{k} \bar{u}_{k} + \frac{1}{2} \tau_{kk}^{R} \end{pmatrix} + \frac{\partial}{\partial x_{j}} \begin{pmatrix} \bar{\rho} \bar{u}_{j} \\ \bar{\rho} \bar{u}_{i} \bar{u}_{j} + \bar{p} \delta_{ij} \\ \frac{1}{2} \bar{\rho} \bar{u}_{k} \bar{u}_{k} \bar{u}_{j} + \bar{E}_{\text{int}} \bar{u}_{j} + \bar{p} \bar{u}_{j} \end{pmatrix} + \frac{\partial}{\partial x_{j}} \begin{pmatrix} \mathcal{M}_{j} \\ \tau_{ij}^{R} \\ \mathcal{K}_{j}^{R} + \mathcal{H}_{j}^{R} \end{pmatrix} = \begin{pmatrix} 0 \\ \bar{\sigma}_{\rho u_{i}} \\ \bar{\sigma}_{E} \end{pmatrix}$$
(2.11)

The SGS terms with the superscript 'R' denote the same SGS terms as in the \tilde{u}_i formulation, but with \bar{u}_i as the resolved-scale velocity. Here,

$$\mathcal{M}_{i} = \overline{\rho u_{i}} - \bar{\rho} \bar{u}_{i}, \quad \tau_{ij}^{R} = \overline{\rho u_{i} u_{j}} - \bar{\rho} \bar{u}_{i} \bar{u}_{j}$$

$$\mathcal{K}_{j}^{R} = \overline{\rho u_{k} u_{k} u_{j}} - \bar{\rho} \bar{u}_{k} \bar{u}_{k} \bar{u}_{j}, \quad \mathcal{H}_{j}^{R} = \overline{(E_{\text{int}} + p) u_{j}} - (\bar{E}_{\text{int}} + \bar{p}) \bar{u}_{j}$$

$$(2.12)$$

The additional SGS quantity \mathcal{M}_i is the SGS mass flux and represents the spatial correlation of density with velocity under the filter operator. It is a measure of the difference between the quantity $\bar{\rho}\bar{u}_i$ and the filtered momentum. With the use of central moments, the SGS stress in this formulation can be written as

$$\tau_{ij}^{R} = \overline{\rho u_i u_j} - \bar{\rho} \bar{u}_i \bar{u}_j = \bar{\rho} \mathcal{T} [u_i, u_j] + \mathcal{T} [\rho, u_i, u_j] + \bar{u}_i \mathcal{T} [\rho, u_j] + \bar{u}_j \mathcal{T} [\rho, u_i]$$
(2.13)

We observe that the term τ_{ij}^{R} like τ_{ij}^{F} , consists of the SGS specific stress, the SGS trivariate moment term, and the SGS mass flux term. However the resolved-scale momentum equation in this formulation also includes the rate of change of SGS mass flux.

In order to understand the unclosed time derivative, we examine the differences between \bar{u}_i and \tilde{u}_i by comparing their respective inviscid transport equations. The governing equation for the Favre-filtered velocity is obtained using the transport equations for the filtered momentum and filtered density. The equation for filtered velocity is obtained by filtering the transport equation for velocity. If we compare the two transport equations, it is seen that in the equation for \bar{u}_i , there exist SGS terms other than the SGS specific stress $\mathcal{T}[u_i, u_j] = \bar{u}_i u_j - \bar{u}_i \bar{u}_j$.

$$\frac{\partial \tilde{u}_i}{\partial t} + \tilde{u}_j \frac{\partial \tilde{u}_i}{\partial x_j} + \frac{1}{\bar{\rho}} \frac{\partial \bar{p}}{\partial x_i} + \frac{1}{\bar{\rho}} \frac{\partial \bar{\rho}(\tilde{u_i u_j} - \tilde{u}_i \tilde{u}_j)}{\partial x_j} = 0$$
(2.14)

$$\frac{\partial \bar{u}_i}{\partial t} + \bar{u}_j \frac{\partial \bar{u}_i}{\partial x_j} + \frac{1}{\bar{\rho}} \frac{\partial \bar{p}}{\partial x_i} + \frac{\partial (\bar{u}_i \bar{u}_j - \bar{u}_i \bar{u}_j)}{\partial x_j} - \mathcal{T} \left[u_i, \frac{\partial u_j}{\partial x_j} \right] - \frac{1}{\bar{\rho}} \mathcal{T} \left[\rho, \frac{1}{\rho} \frac{\partial p}{\partial x_i} \right] = 0 \quad (2.15)$$

These additional SGS terms are associated with dilatation, $\nabla \cdot u$, and pressure acceleration, $\nabla p/\rho$. This is due to the non-conservative nature of velocity in the presence of variable-density effects.

The transport equations for \tilde{u}_i (2.14) and \bar{u}_i (2.15), with the filtered density equation, can be used to derive the transport equation for the SGS mass flux \mathcal{M}_i .

$$\frac{\partial \mathcal{M}_{i}}{\partial t} = \frac{\partial (\overline{\rho u_{i}} - \overline{\rho} \overline{u}_{i})}{\partial t} \\
= -\frac{\partial \overline{\rho u_{i} u_{j}}}{\partial x_{j}} + \overline{u}_{i} \frac{\partial \mathcal{M}_{j}}{\partial x_{j}} + \frac{\partial \overline{\rho} \overline{u}_{i} \overline{u}_{j}}{\partial x_{j}} + \overline{\rho} \frac{\partial \mathcal{T} [u_{i}, u_{j}]}{\partial x_{j}} - \overline{\rho} \mathcal{T} \left[u_{i}, \frac{\partial u_{j}}{\partial x_{j}} \right] - \mathcal{T} \left[\rho, \frac{1}{\rho} \frac{\partial p}{\partial x_{i}} \right] \tag{2.16}$$

For the sake of clarity, we do not consider terms corresponding to viscous molecular transport and work with the inviscid transport equations; including viscous transport term is straight-forward and produces an additional term, $\mathcal{T}\left[\rho, \sigma_{\rho u_i}/\rho\right]$ in (2.16). We note that the filtered momentum equation is a composite equation transporting two physical

variables, \bar{u}_i and \mathcal{M}_i . This implies that a part of the SGS term $\partial_j \tau_{ij}^{\mathrm{R}}$ corresponds to the convection of \mathcal{M}_i . Therefore, the equation for \bar{u}_i can be simplified by decoupling it from the equation for SGS mass flux. Substituting for $\partial_t \mathcal{M}_i$ from (2.16), we obtain

$$\frac{\partial \bar{\rho}\bar{u}_i}{\partial t} + \frac{\partial \mathcal{M}_i}{\partial t} + \frac{\partial \bar{\rho}\bar{u}_i\bar{u}_j}{\partial x_j} + \frac{\partial \bar{p}}{\partial x_i} = \frac{\partial \bar{\rho}\bar{u}_i}{\partial t} + \frac{\partial \bar{\rho}\bar{u}_i\bar{u}_j}{\partial x_j} + \frac{\partial \bar{p}}{\partial x_i} + \mathcal{S}_{\rho u_i}$$
(2.17)

where
$$S_{\rho u_i} = \bar{u}_i S_{\rho} + \bar{\rho} \frac{\partial \mathcal{T} [u_i, u_j]}{\partial x_j} - \bar{\rho} \mathcal{T} \left[u_i, \frac{\partial u_j}{\partial x_j} \right] - \mathcal{T} \left[\rho, \frac{1}{\rho} \frac{\partial p}{\partial x_i} \right]$$
 (2.18)

and
$$S_{\rho} = \frac{\partial \mathcal{M}_{j}}{\partial x_{j}} = \frac{\partial (\overline{\rho u_{j}} - \overline{\rho} \ \overline{u}_{j})}{\partial x_{j}}$$
 (2.19)

Similarly, the filtered energy equation is also a composite equation, where the variable $\frac{1}{2}\tau_{kk}^{\rm R}$ is convected along with $\bar{E}_{\rm int}$ and $\frac{1}{2}\bar{\rho}\bar{u}_k\bar{u}_k$. A part of the SGS term $\partial_j(\mathcal{K}_j^{\rm R}+\mathcal{H}_j^{\rm R})$ in the filtered energy equation therefore corresponds to the convective transport of SGS kinetic energy $\frac{1}{2}\tau_{kk}^{\rm R}$. Similar to the filtered momentum equation, the filtered energy equation can be reduced as well. The transport equations for filtered the kinetic energy, filtered momentum, and filtered velocity are used to obtain the transport equation for $\frac{1}{2}\tau_{kk}^{\rm R}=\frac{1}{2}(\bar{\rho}u_ku_k-\bar{\rho}u_k\bar{u}_k)$.

$$\frac{1}{2} \frac{\partial}{\partial t} \left(\overline{\rho u_k u_k} - \bar{\rho} \bar{u}_k \bar{u}_k \right) = \frac{1}{2} \frac{\partial \overline{\rho u_k u_k}}{\partial t} - \frac{1}{2} \bar{u}_k \frac{\partial \bar{\rho} \bar{u}_k}{\partial t} - \frac{1}{2} \bar{\rho} \bar{u}_k \frac{\partial \bar{u}_k}{\partial t} \\
= -\frac{\partial}{\partial x_j} \left(\frac{1}{2} \overline{\rho u_k u_k u_j} + \overline{p u_j} \right) + \mathcal{T} \left[p, \frac{\partial u_j}{\partial x_j} \right] + \frac{\partial \bar{p} \bar{u}_j}{\partial x_j} \\
+ \frac{1}{2} \frac{\partial \bar{\rho} \bar{u}_k \bar{u}_k \bar{u}_j}{\partial x_j} + \bar{u}_k \mathcal{S}_{\rho u_k} - \frac{1}{2} \bar{u}_k \bar{u}_k \mathcal{S}_{\rho}$$
(2.20)

Substituting $\partial_t \frac{1}{2} \tau_{kk}^{\rm R}$ in the filtered total energy equation, we obtain

$$\frac{\partial}{\partial t} \left(\bar{E}_{int} + \frac{1}{2} \bar{\rho} \bar{u}_k \bar{u}_k + \frac{1}{2} \tau_{kk}^{F} \right) + \frac{\partial}{\partial x_j} \left(\bar{E}_{int} u_j + \bar{\rho} u_k u_k u_j + \bar{p} u_j \right)
= \frac{\partial}{\partial t} \left(\bar{E}_{int} + \frac{1}{2} \bar{\rho} \bar{u}_k \bar{u}_k \right) + \frac{\partial}{\partial x_j} \left(\bar{E}_{int} \bar{u}_j + \frac{1}{2} \bar{\rho} \bar{u}_k \bar{u}_k \bar{u}_j + \bar{p} \bar{u}_j \right) + \mathcal{S}_E$$
(2.21)

where the SGS terms in the transport of the quantity $\bar{E}_{\rm int} + \frac{1}{2}\bar{u}_k\bar{u}_k$ are

$$S_E = \frac{\partial}{\partial x_j} \left(\mathcal{T} \left[E_{\text{int}}, u_j \right] \right) + \mathcal{T} \left[p, \frac{\partial u_j}{\partial x_j} \right] + \bar{u}_k S_{\rho u_k} - \frac{1}{2} \bar{u}_k \bar{u}_k S_{\rho}$$
 (2.22)

Thus, the Reynolds-filtered LES equations can then be written as:

$$\frac{\partial}{\partial t} \begin{pmatrix} \bar{\rho} \\ \bar{\rho}\bar{u}_i \\ \bar{E}_{\text{int}} + \frac{1}{2}\bar{\rho}\bar{u}_k\bar{u}_k \end{pmatrix} + \frac{\partial}{\partial x_j} \begin{pmatrix} \bar{\rho}\bar{u}_j \\ \bar{\rho}\bar{u}_i\bar{u}_j + \bar{p}\delta_{ij} \\ \frac{1}{2}\bar{\rho}\bar{u}_k\bar{u}_k\bar{u}_j + \bar{E}_{\text{int}}\bar{u}_j + \bar{p}\bar{u}_j \end{pmatrix} + \begin{pmatrix} \mathcal{S}_{\rho} \\ \mathcal{S}_{\rho u_i} \\ \mathcal{S}_E \end{pmatrix} = \begin{pmatrix} 0 \\ \bar{\sigma}_{\rho u_i} \\ \bar{\sigma}_E \end{pmatrix} \tag{2.23}$$

where the SGS contribution to the governing equations is:

$$S_{\rho} = \frac{\partial \mathcal{T}\left[\rho, u_{j}\right]}{\partial x_{j}} \tag{2.24}$$

$$S_{\rho u_i} = \bar{u}_i S_{\rho} + \bar{\rho} \frac{\partial \mathcal{T}[u_i, u_j]}{\partial x_j} - \mathcal{T} \left[\rho, \frac{1}{\rho} \frac{\partial p}{\partial x_i} \right] - \bar{\rho} \, \mathcal{T} \left[\nabla \cdot u, u_i \right]$$
 (2.25)

$$S_E = \bar{u}_i S_{\rho u_i} - \frac{1}{2} \bar{u}_i \bar{u}_i S_\rho + \frac{\partial \mathcal{T} [E_{\text{int}}, u_j]}{\partial x_j} + \mathcal{T} [\nabla \cdot u, p]$$
(2.26)

The conservation-law form of the closed convective terms is maintained and the non-conservative SGS source terms arise as a consequence of choosing to solve for the filtered velocity instead of the filtered momentum. The unclosed SGS terms are:

• SGS mass flux	$\mathcal{T}\left[\rho, u_i\right] = \overline{\rho u_i} - \bar{\rho} \bar{u}_i$
• SGS specific stress	$\mathcal{T}\left[u_i, u_j\right] = \overline{u_i u_j} - \bar{u}_i \bar{u}_j$
• SGS dilatational flux	$\mathcal{T}\left[\nabla \cdot u, u_i\right] = \overline{(\nabla \cdot u)u_i} - (\nabla \cdot \bar{u})\bar{u}_i$
• SGS pressure work	$\mathcal{T}\left[\nabla\cdot u,p\right] = \overline{(\nabla\cdot u)p} - (\nabla\cdot \bar{u})\bar{p}$
• SGS pressure acceleration	$\mathcal{T}\left[\rho, \nabla_i p/\rho\right]/\bar{\rho} = -(\overline{\nabla_i p/\rho} - \nabla_i \bar{p}/\bar{\rho})$
• SGS internal energy flux	$\mathcal{T}\left[E_{\mathrm{int}}, u_{i}\right] = \overline{E_{\mathrm{int}}u_{i}} - \bar{E}_{\mathrm{int}}\bar{u}_{i}$

All of the SGS terms satisfy the principle of Galilean invariance. The new SGS terms corresponding to variable-density effects not previously analyzed in the LES literature are the SGS pressure acceleration and the SGS dilatational flux. The SGS pressure acceleration arises due to the non-linear interaction between pressure gradient and density. The SGS dilatational flux arises from the non-linear product of dilatation and velocity. We observe its similarity to the SGS pressure work, commonly referred to as the SGS pressure-dilatation. SGS pressure work has been studied extensively in the literature, because it appears in the transport equation of SGS kinetic energy, irrespective of the choice of the resolved-scale velocity variable. It should also be noted that in a multicomponent reacting flow, \bar{p} cannot be obtained directly from $\bar{E}_{\rm int}$. In flows that involve non-constant $\partial p/\partial E_{\rm int}|_{\rho}$, such as in the case of real/dense gas effects or multi-component mixture of gases with different heat capacity ratio, the term $\bar{p} - p(E_{\rm int}, \bar{\rho})$ requires closure as well. In such a case, non-linear relation between pressure and total internal energy effects the momentum equation through the filtered pressure. In this paper, we consider a single gas that obeys the ideal gas law. Therefore, the SGS term $\bar{p} - p(\bar{E}_{int}, \bar{\rho})$ does not appear in the resolved-scale momentum equation.

The primary advantage of the new equations over the conventional Reynolds-filtered formulation is the presence of a framework in which SGS contributions arising from spatial and Lagrangian density variations may be explicitly quantified. The simplified nature of the SGS terms avoids the trivariate central moment $\mathcal{T}\left[\rho,u_{i},u_{j}\right]$ in the filtered momentum equation and the quadrivariate central moment $\mathcal{T}\left[\rho,u_{k},u_{k},u_{j}\right]$ in the energy equation. This is a result of decoupling the transport equation for the SGS mass flux \mathcal{M}_{i} and the SGS kinetic energy $\frac{1}{2}\tau_{kk}^{\mathrm{R}}$ from the filtered momentum and the filtered energy equations. The decoupling concept for the energy equation is not restricted to a Reynolds-filtered formulation. For Favre-filtered equations, solving for the variable $\bar{E}_{\mathrm{int}} + \frac{1}{2}\bar{\rho}\tilde{u}_{k}\tilde{u}_{k}$ (referred to as computable energy in Vreman 1995), instead of the filtered total energy $\bar{E}_{\mathrm{int}} + \frac{1}{2}\bar{\rho}\tilde{u}_{k}\tilde{u}_{k}$ removes $\mathcal{K}_{j}^{\mathrm{F}}$. Following a procedure similar to (2.20), we may obtain the following Favre-filtered kinetic energy equation in which no quadrivariate central moments appear.

$$\frac{\partial}{\partial t} \left(\frac{\bar{\rho} \tilde{u}_k \tilde{u}_k}{2} + \bar{E}_{int} \right) + \frac{\partial}{\partial x_j} \left(\overline{E}_{int} u_j + \frac{\bar{\rho} \tilde{u}_k \tilde{u}_k \tilde{u}_j}{2} + \bar{p} \tilde{u}_j \right) + \tilde{u}_i \frac{\partial \tau_{ij}^{\mathrm{F}}}{\partial x_j} + \left(\overline{p} \frac{\partial u_j}{\partial x_j} - \bar{p} \frac{\partial \tilde{u}_j}{\partial x_j} \right) = \bar{\sigma}_E$$
(2.27)

2.3. Filtered vorticity equation

The resolved-scale vorticity computed from the equations is a consequence of the choice of the resolved-scale velocity. While the Reynolds-filtered formulation computes filtered vorticity $\bar{\omega}_i$, in the case of Favre-filtered velocity, the resolved-scale vorticity variable is $\omega_i^{\rm F} = \nabla \times \bar{\rho} u_i / \bar{\rho}$. This is different from the filtered vorticity $\bar{\omega}_i$, or even the Favre-filtered vorticity $\tilde{\omega}_i$. Consider the filtered inviscid vorticity equation with the SGS terms represented as central moments.

$$\frac{\partial \bar{\omega}_{i}}{\partial t} + \frac{\partial \bar{\omega}_{i} \bar{u}_{j}}{\partial x_{j}} + \frac{\partial \mathcal{T} \left[\omega_{i}, u_{j}\right]}{\partial x_{j}} = \bar{\omega}_{j} \frac{\partial \bar{u}_{i}}{\partial x_{j}} + \mathcal{T} \left[\omega_{j}, \frac{\partial u_{i}}{\partial x_{j}}\right] - \epsilon_{ijk} \left(\frac{\partial (\overline{1/\rho})}{\partial x_{j}} \frac{\partial \bar{p}}{\partial x_{k}}\right) + \mathcal{T} \left[\frac{\partial (1/\rho)}{\partial x_{j}}, \frac{\partial p}{\partial x_{k}}\right] \right) \tag{2.28}$$

The SGS contributions to vorticity flux, vortex stretching, and baroclinic torque can be seen to appear separately. We observe that the curl of the SGS pressure acceleration is the SGS baroclinic torque.

$$-\epsilon_{ijk}\mathcal{T}\left[\frac{\partial}{\partial x_j}\left(\frac{1}{\rho}\right), \frac{\partial p}{\partial x_k}\right] = \epsilon_{ijk}\frac{\partial}{\partial x_j}\left(\frac{1}{\bar{\rho}}\mathcal{T}\left[\rho, \frac{1}{\rho}\frac{\partial p}{\partial x_k}\right]\right)$$
(2.29)

The SGS acceleration field contributes to the filtered vorticity, and more generally to the entire filtered velocity gradient tensor. The symmetric part of the SGS pressure acceleration gradient tensor $\partial_j(\mathcal{T}\left[\rho,\partial_k p/\rho\right]/\bar{\rho})$ appears as a source term in the filtered strain rate \bar{S}_{ij} equation. SGS pressure acceleration, due its dependence on both pressure and density field, can distinguish between entropic and acoustic density fluctuations. This can be important for modeling (Hamba 1999; Rubinstein & Erlebacher 1997).

Therefore, we see that the curl of the Reynolds-filtered and Favre-filtered velocities represent physically different resolved-scale vorticity variables. In particular, the subgrid-scale baroclinic torque affects Reynolds-filtered vorticity $\bar{\omega}_i$, but does not explicitly affect ω_i^F .

2.4. Filtered scalar advection equation

It is important to discuss scalar advection equation in the context of variable-density flows. For example, flows that involve multicomponent mixing and combustion require advection of species densities. When a combustion model is used, a reaction progress variable is advected. The filtered inviscid scalar advection equations with \tilde{u}_i and \bar{u}_i are

$$\frac{\partial \bar{\rho}\tilde{c}}{\partial t} + \frac{\partial \bar{\rho}\tilde{u}_{j}\tilde{c}}{\partial x_{j}} + \frac{\partial C_{j}}{\partial x_{j}} = \overline{\rho}\Omega_{c}$$
(2.30)

$$\frac{\partial \bar{\rho}\tilde{c}}{\partial t} + \frac{\partial \bar{\rho}\bar{u}_{j}\tilde{c}}{\partial x_{j}} + \frac{\partial \mathcal{T}\left[\rho c, u_{j}\right]}{\partial x_{j}} = \overline{\rho\Omega_{c}}$$

$$(2.31)$$

where scalar c is the advected variable. Ω_c represents the source term in the transport equation of the scalar c. The unclosed term in the Favre-filtered velocity scalar equation

can be expressed with central moments similar to the subgrid-scale stress $\tau_{ij}^{\rm F}$

$$C_j = \overline{\rho u_j c} - \bar{\rho} \tilde{u}_j \tilde{c} = \bar{\rho} (\widetilde{cu}_j - \tilde{c} \tilde{u}_j)$$
(2.32)

$$= \bar{\rho} \mathcal{T}[c, u_j] + \mathcal{T}[\rho, u_j, c] - \frac{1}{\bar{\rho}} \mathcal{T}[\rho, u_j] \mathcal{T}[\rho, c]$$
(2.33)

In the equations above, the Favre-filtered scalar is transported. It is also possible to derive the transport equation for the filtered scalar and express the equation in a conservation law form:

$$\frac{\partial \bar{\rho}\bar{c}}{\partial t} + \frac{\partial \bar{\rho}\bar{u}_j\bar{c}}{\partial x_j} + \mathcal{S}_{\rho c} = \bar{\rho}\bar{\Omega}_c \tag{2.34}$$

where the subgrid-scale contribution $\mathcal{S}_{\rho c}$ is expressed in the form of central moments as

$$S_{\rho c} = \bar{\rho} \frac{\partial \mathcal{T}[c, u_j]}{\partial x_j} + \bar{c} S_{\rho} - \bar{\rho} \mathcal{T} \left[c, \frac{\partial u_j}{\partial x_j} \right]$$
 (2.35)

Equation (2.34) is obtained by decoupling the inviscid transport equation for $\mathcal{T}[\rho, c]$ from (2.30), similar to the procedure we adopt for the resolved-scale momentum and the energy equations. We observe that usage of filtered velocity does not involve the trivariate moment $\mathcal{T}[\rho, u_j, c]$ in the unclosed terms. In the case of Favre-filtered scalar and the filtered velocity, the effect of density appears in subgrid-scale conserved scalar flux $\mathcal{T}[\rho c, u_j]$. If the filtered scalar is transported, the effect of SGS mass flux and SGS dilatation can be represented explicitly.

3. Direct numerical simulations

We carry out direct numerical simulations of decaying isotropic compressible turbulence to study variable-density and dilatation effects on the flow. The data from the DNS will be filtered to evaluate the relative importance of the variable-density SGS terms. Two flow cases are investigated, as listed in Table 1. The first case is canonical decaying compressible turbulence where initial thermodynamic fluctuations are homentropic, i.e. the flow has spatially uniform entropy. The second case is compressible variable-density decaying turbulence, where the initial density field is isotropic, inhomogeneous, and corresponds to a double- δ probability distribution function. In the first case, density fluctuations arise primarily out of compressibility, while in the second, density fluctuations are primarily a consequence of the mixing of fluid of varying density. A variant of the second case with stronger initial density fluctuations is also simulated. In these simulations, the double- δ pdf density field initialization corresponds to thermal inhomogeneity which is different from binary mixing between two different fluid species with associated species mass diffusion. Therefore, Schmidt-number effects are outside the scope of these simulations. Since the imprints of initial conditions in triperiodic decaying compressible flows can persist throughout the simulation time (Ristorcelli & Blaisdell 1997), the initial conditions in the current simulations are carefully designed to avoid impulsive forcing of the flow field that might corrupt the high-order statistics.

3.1. Simulation setup and numerical method

We solve the compressible Navier-Stokes equations on a triperiodic domain with initialization for the variables ρ , u_i , p. The ideal gas law $p = \rho RT$ is used to compute the temperature field. Transport properties such as viscosity are taken to be constant, to avoid the influence of variable-density fluctuations on viscous transport processes. The

Table 1. Primary flow-cases simulated for subgrid-scale analysis			
		Initial condition	Atwood number
	Case 1	IC1 (homentropic ρ fluctuations)	-
	Case 2a	IC2 (isotropic double- $\delta~\rho$ pdf)	0.4
	Case 2b	IC2 (isotropic double- $\delta \rho$ pdf)	0.7

viscous terms in the momentum and energy equations are $\sigma_{\rho u_i} = -\mu(\partial_j S_{ij} - 2/3 \partial_j S_{kk} \delta_{ij})$ and $\sigma_E = -c_p \mu/Pr \partial_j T$, respectively. S_{ij} is the strain rate tensor, and c_p is the specific heat capacity. We assume a calorically perfect gas with constant $c_p = 1.003 \text{ kJ/kg K}$ and a Prandtl number of 0.72.

$$\frac{\partial}{\partial t} \begin{pmatrix} \rho \\ \rho u_i \\ \frac{1}{2} \rho u_k u_k + E_{\text{int}} \end{pmatrix} + \frac{\partial}{\partial x_j} \begin{pmatrix} \rho u_j \\ \rho u_i u_j + p \delta_{ij} \\ \frac{1}{2} \rho u_k u_k + E_{\text{int}} u_j + p u_j \end{pmatrix} + \begin{pmatrix} 0 \\ \sigma_{\rho u_i} \\ \sigma_E \end{pmatrix} = \begin{pmatrix} 0 \\ 0 \\ 0 \end{pmatrix}$$
(3.1)

A triperiodic grid with 512 points in each co-ordinate direction is used for the simulations. Three cases are considered (Table 1) with turbulent Mach number M_t of 0.3, which is chosen as representative of high-speed turbulent boundary layers (Lagha et~al.~2011). The initial velocity field is identical for all cases, and is initialized by extracting the solenoidal velocity component from a precursor simulation of compressible decaying turbulence simulation whose velocity derivative skewness has saturated to a value close to 0.5. Saturation in skewness implies that the rate of vorticity production via vortex stretching has stabilized and the flow has evolved from an artificial state into a turbulent state with realistic non-linear dynamics. The precursor simulation therefore ensures that the flows initialized in this study are closer to a realistic turbulent flow compared to a random isotropic velocity field. The precursor simulation is initialized with a $k^2 \exp(-2(k/k_0)^2)$ radial spectrum with $Re_{\lambda} = 100$, $M_t = 0.3$, $k_0/L = 6$ and simulated to $t/t_{\rm eddy} = 3.0$.

Initial density, pressure, and temperature fields are initialized in two different ways denoted by IC1 and IC2. In IC1, the initial pressure field is obtained from the incompressible Poisson equation using the volume-averaged density. The density field is then initialized with $p/\rho^{\gamma} = \langle p \rangle / \langle \rho \rangle^{\gamma}$ (Samtaney et al. (2001); Ristorcelli & Blaisdell (1997)). Note that only the solenoidal velocity field from the precursor simulation is used for initialization. This is because with IC1 thermodynamic fields, the time evolution of mean dilatation variance with zero initial dilatation is nearly identical to that from a non-zero initial dilatation obtained from small parameter expansion about M_t (Ristorcelli & Blaisdell (1997)). The two curves from zero and non-zero initial dilatation are found to nearly overlap for $t/t_{\rm eddy} > 0.3$. The turbulent kinetic energy decay in compressible turbulence using IC1 is compared to results from Samtaney et al. (2001) in the Appendix.

IC2 corresponds to an isotropic double- δ distribution of the density field with the volume divided into two regions of densities ρ_1 and ρ_2 , with a smooth interface. Similar scalar fields have been used previously in the work of Livescu & Ristorcelli (2007) and Sandoval (1995). The scalar field is generated with non-zero spectral content for $2 \leq kL \leq 4$, where L is the length of the periodic domain. To generate a smooth interface, the field is filtered with an exponential filter with $k_cL = 4$, resulting in a ρ pdf that deviates slightly from a strict double- δ distribution. Smoothing the ρ interface changes

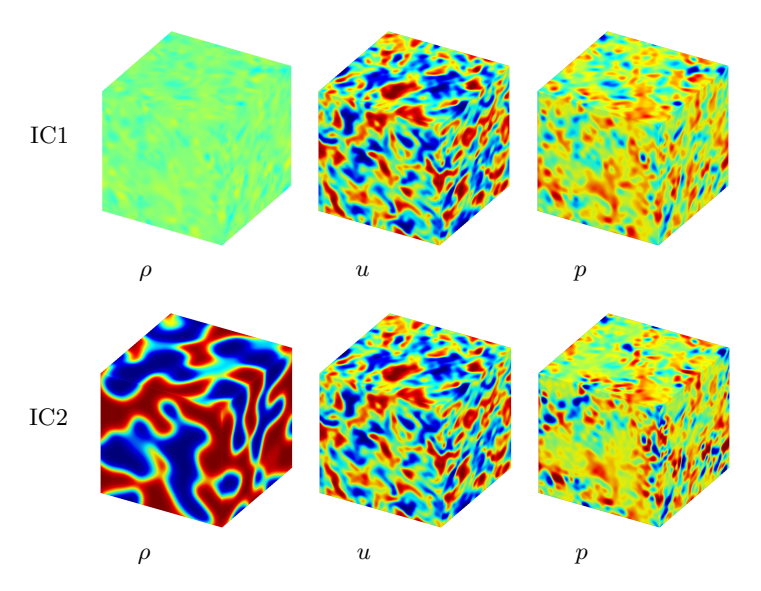


FIGURE 1. DNS initialization: ρ , u, p fields are shown.

the mean and variance of the density distribution from 1.0 and 0.25 to 1.017 and 0.235, respectively. The Atwood number $A=(\rho_2+\rho_1)/(\rho_2-\rho_1)$ is an important parameter in quantifying the strength of hydrodynamic instability in stratified flows; a volumetric mean density $\langle \rho \rangle = 1.0$ is used to calculate ρ_1 and ρ_2 . Cases 2a and 2b use IC2, but differ in the Atwood number. Case 2b has a larger Atwood number than Case 2a, and as expected, exhibits more pronounced variable-density effects. The largest value of Atwood number considered here corresponds to a density ratio of approximately 6, which is a typical of light/heavy fluid mixing in industrial applications. Larger density ratios exist in combustion and multiphase systems, and are expected to produce stronger variable-density effects. The pressure in IC2 is determined by solving the inviscid variable-density Poisson equation. This equation is obtained by ensuring that the initial conditions do not provide a source of Lagrangian change in fluid density, $D(\partial_j u_j)/Dt = 0$. The pressure at time t = 0 therefore satisfies

$$\frac{\partial}{\partial x_i} \left(\frac{1}{\rho} \frac{\partial p}{\partial x_i} \right) = -\frac{\partial u_j}{\partial x_i} \frac{\partial u_i}{\partial x_j} \tag{3.2}$$

We restrict the initial u_i , ρ fields to large length scales. The velocity field from the precursor simulation and the generated density field are filtered using a sharp-spectral filter with $k_cL=32$. This ensures that the small scales in the density and velocity fields develop from the initial conditions together via vortex stretching and baroclinic torque. The viscosity is specified such that the initial Taylor length scale Reynolds number Re_{λ} is 500. Re_{λ} is large because the initial velocity spectrum is non-zero at low wavenumbers kL < 32, resulting in a large initial Taylor length scale λ . After the transient, the energy spectrum becomes broadband and Re_{λ} decreases. At $t/t_{\rm eddy}=3$, the Taylor length scale Reynolds number reduces to $Re_{\lambda}=85$. The fields corresponding to the initial conditions are visualized in figure 1.

A finite-volume scheme is employed to solve 3.1. The convective flux is evaluated using a stable low-dissipation scheme based on the kinetic-energy consistent method developed by Subbareddy & Candler (2009). A gradient reconstruction method described in Subbareddy et al. (2014) is used to make the symmetric part of the convective flux

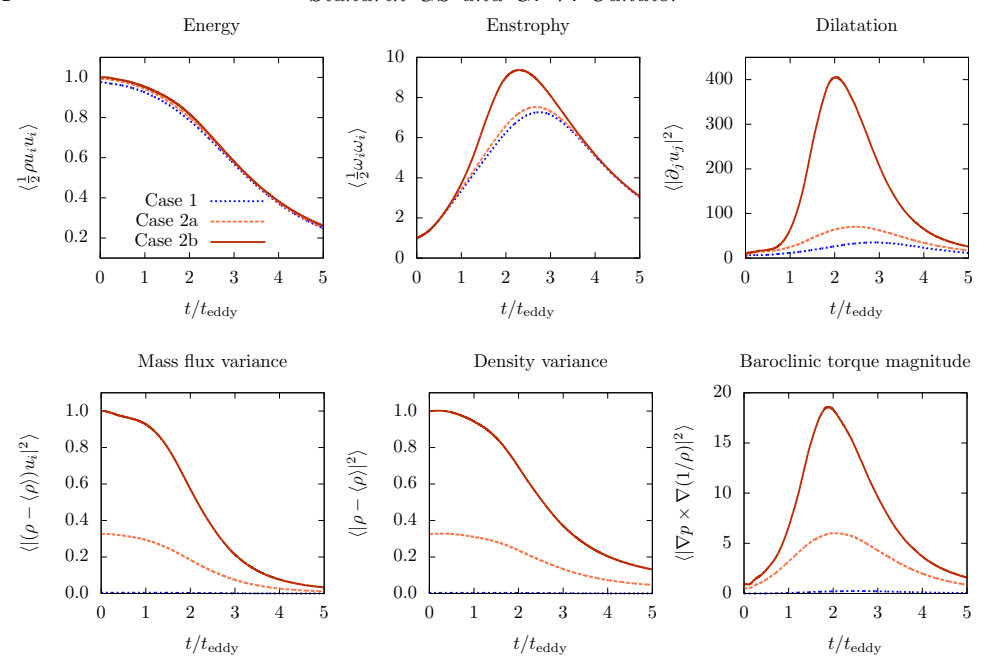


Figure 2. Time history of volume averaged quantities.

formally sixth-order accurate. In regions of strong compression (shocklets), a Ducros-type shock sensor adds dissipation to the convective flux using the non-symmetric part of the modified Steger-Warming flux-vector splitting scheme. The details of the flux scheme can be found in Candler et al. (2015) and MacCormack (2014). The viscous fluxes are computed using a second-order central scheme and use compact stencil second-order least-squares gradients. The low-storage third-order accurate strong-stability preserving Runge-Kutta scheme (Gottlieb et al. 2001) is used for time integration. A CFL number of 0.7 based on the local fast characteristic wave speed is used.

3.2. Time histories and spatial statistics

Volume-averaged statistics from the three cases simulated are shown in figure 2. Time histories of six physical quantities are plotted: (a) kinetic energy, (b) enstrophy, (c) dilatation variance, (d) mass flux variance, (e) density variance, and (f) baroclinic torque variance. The volume averages of dilatation, mass flux and baroclinic torque are numerically close to zero, and hence, variances of these quantities are plotted. All the curves are normalized by the value corresponding to Case 2b at time t=0. While the volume-averaged kinetic energy curves nearly overlap, quantities based on velocity gradients, namely the enstrophy and dilatation variance, exhibit prominent differences during $1 \le t/t_{\rm eddy} \le 4$. This occurs when small velocity scales are produced by vortex stretching and variable-density mixing effects are active. Later, when mixing homogenizes the density field, the curves of kinetic energy, enstrophy and dilatation variance for Cases 2a and 2b begin to converge with the Case 1 curves.

Velocity-gradient-based statistics are found to be more strongly affected by variable-density effects. In the case of enstrophy, the differences can be attributed to production of vorticity by baroclinic torque, which is the curl of the pressure-gradient acceleration. Baroclinic-torque-generated vorticity is further stretched by the background strain, thus compounding the enstrophy generation process. We also note that the differences in

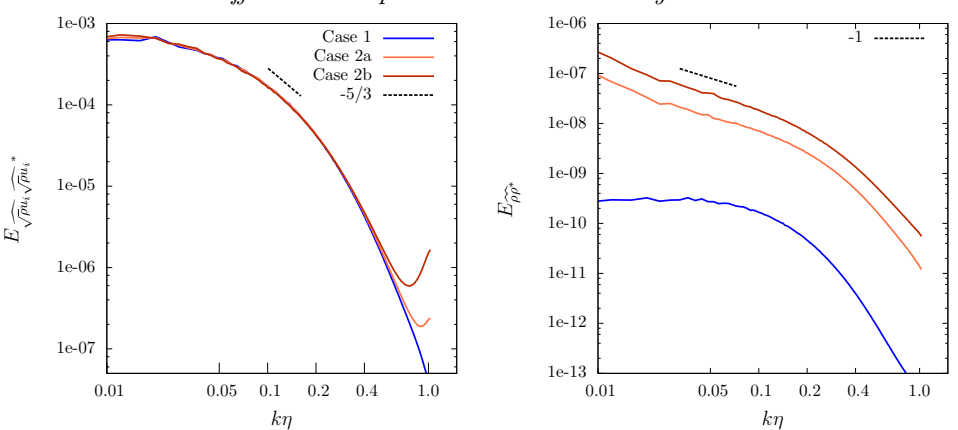


FIGURE 3. Three-dimensional shell-averaged radial spectra of kinetic energy (left) and energy spectral density of the density (right) at $t/t_{\rm eddy} = 3.0$.

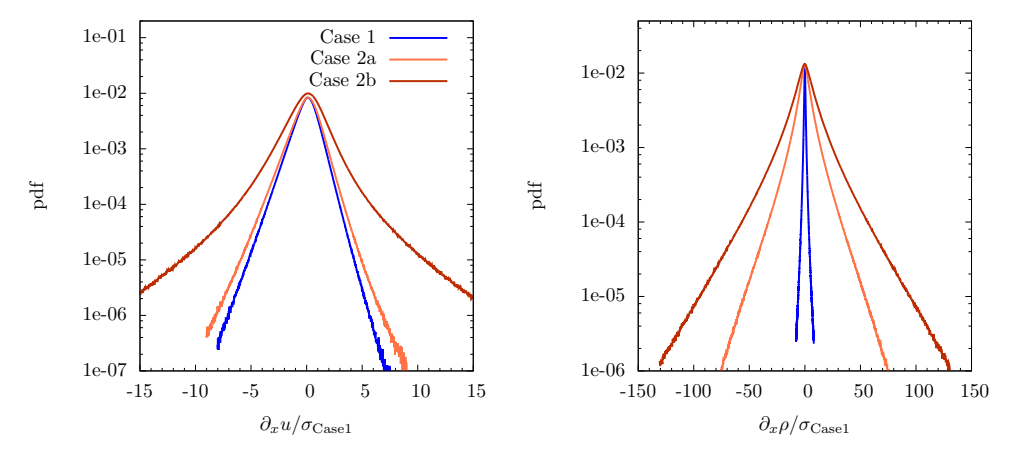


FIGURE 4. Probability distribution functions of x-gradients of x component of velocity (left) and the density (right) fields.

the curves are discernible only after one eddy turnover time, indicating the absence of impulsively-generated enstrophy by the initial conditions. The increase in dilatation variance (figure 2c) in Cases 2a and 2b can be explained by the pressure-gradient acceleration. The pressure-gradient acceleration tensor $A_{ij} = \partial_j(\partial_i p/\rho)$ appears in the velocity gradient transport equation. The antisymmetric part $A_{ij} - A_{ji}$ is associated with baroclinic torque and the corresponding term in the dilatation rate equation is the trace of the tensor A_{ii} . The symmetric part $A_{ij} + A_{ji}$ contributes to the rate of change of the strain rate tensor. The fluctuating mass flux variance and the density fluctuation variance decay monotonically, but have transience that lasts approximately two eddy turnover times, marked by an inflection point in their respective curves. The fluctuating mass flux is also the mean fluctuating Favre-filtered velocity, and represents the spatial correlation of the density and the velocity fields. The initial density variance in Case 1 is seen to be extremely small relative to Cases 2a and 2b, and suggests that the variable-density effects in compressible decaying turbulence are expected to be small for $M_t = 0.3$.

The kinetic energy radial spectra and the energy spectral density of the density field at $t/t_{\rm eddy} = 3.0$ are plotted in figure 3. The flow field at this time contains a small

inertial subrange with a $k^{-5/3}$ slope present approximately between $0.2 \ge k\eta \ge 0.1$. The presence of initial thermal-density inhomogeneity increases the content at small velocity scales, but the $k^{-5/3}$ spectrum is preserved. Increasing strength of density fluctuations leads to increased rate of kinetic energy transfer to higher wavenumbers. This is also reflected in the aliasing error that develops at high wavenumbers due to the use of a low-dissipation central numerical scheme in the simulations. The density field spectrum shows that the content in the large scales for Case 1 is relatively flat ($\sim k^0$), while Cases 2a and 2b, which involve mixing of variable-density fluids, exhibit a k^{-1} behavior at low wavenumbers. This may be interpreted as the Batchelor k^{-1} viscous-convective scaling in the high Schmidt number limit as the effective diffusivity for density is zero (Donzis et al. 2010).

Figure 4 shows the effect of variable-density mixing on the intermittency of the flow fields. Probability distribution functions of x-gradients of the x component of the velocity and density are plotted. The mean values have been subtracted and the x-axis is scaled with the standard deviation for Case 1. Variable-density effects are seen to increase the probability of occurrence of tail events and have distributions with larger standard deviation. The $\partial_x u$ and $\partial_x \rho$ pdfs show that all cases have a high degree of super-Gaussian (leptokurtic) character, indicating the presence of intermittency representative of high Re turbulence (Schumacher $et\ al.\ 2014$). The kurtosis of the $\partial_x u$ and $\partial_x \rho$ fields in Case 1 is 18.8 and 22.7, respectively. In Case 2b, the value of kurtosis for both distributions reduces to 13.0 and 16.7, respectively, due to increased probability of the occurrence of tail events. In comparison, the kurtosis of a Gaussian distribution is 3.

4. Variable-density subgrid-scale analysis

In this section, we explicitly filter the DNS flow fields to study the SGS terms that appear in the Favre-filtered and Reynolds-filtered momentum equations. The first subsection compares the two resolved-scale velocity fields in Fourier and physical space. The second subsection compares the importance of the variable-density SGS terms with respect to the constant-density SGS terms. Central moments that involve ρ and $\nabla \cdot u$ as one of the variables under the filter operator are referred to as variable-density SGS terms. Terms that involve the SGS specific stress $\mathcal{T}[u_i,u_j]=\overline{u_iu_j}-\bar{u}_i\bar{u}_j$ are referred to as constant-density SGS terms. This is the first study that computes the effect of the small-scale density variations on large-scale momentum in compressible turbulent mixing of variable-density fluids. We restrict the results to a budget analysis, and no a priori assessment of SGS closures is conducted. Similarly, as aforementioned, the effect of implicit filtering associated with an LES discretization is not discussed.

The time histories of dilatation and enstrophy suggest that the flows reach a state of decay after two eddy turnover times. Therefore, we carry out the variable-density SGS analysis of the instantaneous flow field at $t/t_{\rm eddy}=3.0$. The conclusions from the analysis are not sensitive to the time chosen in the decay regime. An exponential filter with $k_c\eta=0.12$ is used to filter the fields, and all filtering operations are carried out in Fourier space. The value of 0.12 is chosen so that the cutoff wavenumber lies in the inertial subrange and approximately 82% of the kinetic energy is resolved. The effect of filter type and the choice of filter width is discussed in the Appendix. It is found that the relative importance of the variable-density SGS terms is not sensitive to either of these parameters.

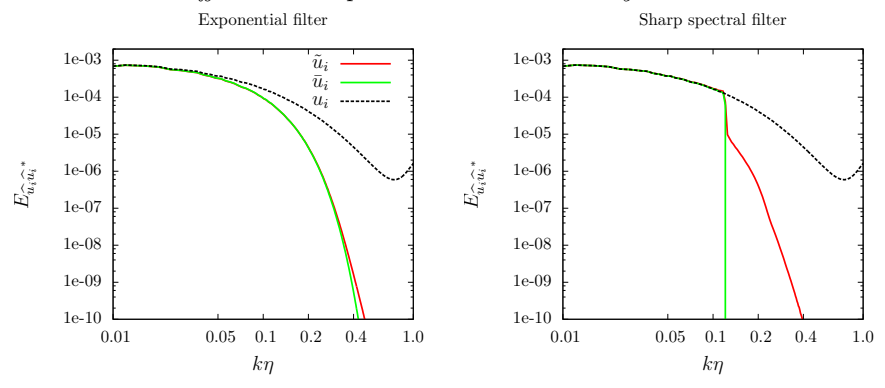


FIGURE 5. Resolved-scale velocity radial spectra from Case 2b filtered with $k_c \eta = 0.12$ with different filters: Favre-filtered velocity \tilde{u}_i and filtered velocity \bar{u}_i are compared.

4.1. Comparison of Reynolds-filtered and Favre-filtered velocity fields

The flow field corresponding to Case 2b with Atwood number of 0.7 is filtered to assess the differences between the \tilde{u}_i and \bar{u}_i velocity fields. The spectral content for both resolved-scale variables is found to be nearly identical for this case, with \tilde{u}_i having slightly larger specific energy at wavenumbers beyond the filter cutoff (figure 5). This is true for the exponential and the sharp spectral filter. We also compare the filtered vorticity $\bar{\omega}_i$ and the curl of the Favre-filtered velocity $\nabla \times \tilde{u}_i$ in Fourier and physical space (figure 6 left). The curl of the Favre-filtered velocity $\omega_i^F = \nabla \times \tilde{u}_i$ is referred to as pseudo-vorticity in Chakraborty et al. (2017). We also note that pseudo-vorticity ω_i^F is not the Favre-filtered vorticity $\tilde{\omega}_i$. The differences in the spectral content of the filtered vorticity and pseudo-vorticity are found to be similar to the differences in the spectral content of the velocity fields, except they are amplified because $E_{\tilde{\omega}_i \tilde{\omega}_i^*} \sim k^2 E_{\tilde{u}_i \tilde{u}_i^*}$

In physical space, the pdf of the normalized difference between the \bar{u}_i and \tilde{u}_i gradient fields is plotted. It is found that the difference between $\bar{\omega}_i$ and $\omega_i^{\rm F}$ can exceed 100% in different regions of the flow. This is seen in figure 6 (right), where $|\bar{\omega}_i| - |\omega_i^{\rm F}| > |\bar{\omega}_i|$ (area under the solid curve beyond horizontal-axis value of 1.0). The differences between the magnitude of \bar{S}_{ij} and $S_{ij}^{\rm F} = 1/2(\partial_i \tilde{u}_j + \partial_j \tilde{u}_i)$ can also be large, but are relatively less pronounced than in the case of vorticity variables. In summary, the spectral content of the Favre-filtered and the Reynolds-filtered velocity fields in Case 2b do not exhibit strong disparities in the decay stage. However, differences in the resolved-scale velocity gradient fields in physical space are non-negligible.

4.2. Variable-density SGS terms in resolved-scale momentum equation

Subgrid-scale terms in the resolved-scale momentum equation are computed using the DNS fields at $t/t_{\rm eddy}=3.0$ with an exponential filter of $k_c\eta=0.12$. The SGS terms involving density ρ and dilatation $\nabla \cdot u$ in the central moments are of primary interest. The SGS specific stress $\mathcal{T}[u_i,u_j]$ serves as the reference for comparison. The analysis is unique because the terms appearing in the resolved-scale momentum equation are considered, as opposed to terms appearing in the transport equations of SGS kinetic energy, SGS stress, or other second-moment SGS terms. The resolved-scale momentum equations corresponding to both the variables, $\partial_t \bar{\rho} \bar{u}_i$ and $\partial_t \bar{\rho} \bar{u}_i$ are considered; each equation has its own set of SGS terms.

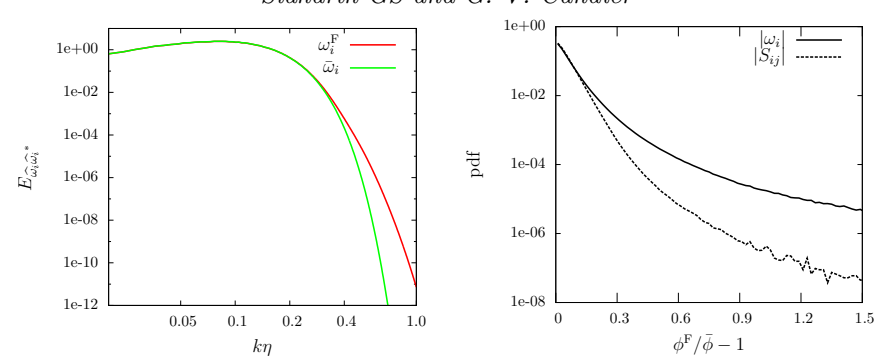


FIGURE 6. Comparison of filtered vorticity $\bar{\omega}_i$ and the curl of Favre-filtered velocity $(\omega_i^F = \nabla \times \tilde{u}_i \neq \tilde{\omega}_i)$ (left) and the relative difference between \bar{u}_i and \tilde{u}_i gradient quantities in physical space (right).

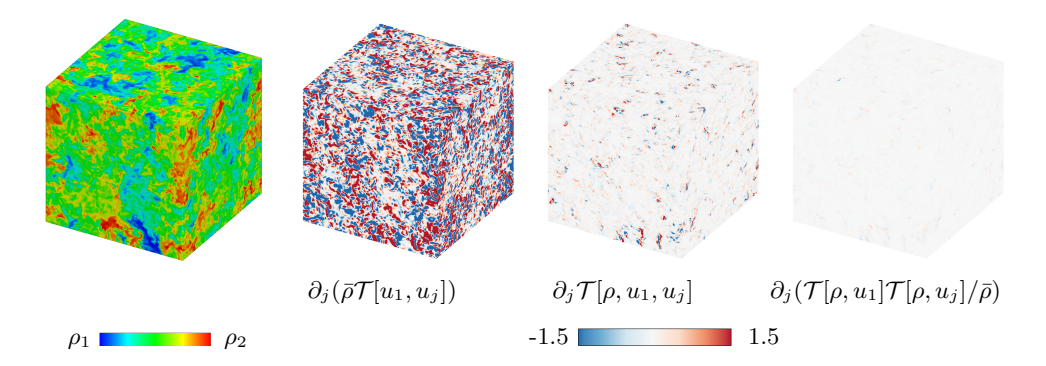


FIGURE 7. Case 2b: instantaneous density field at $t/t_{\rm eddy}=3$ (left), and snapshots of fields corresponding to the SGS terms in $\partial_t \bar{\rho} \tilde{u}_1$ equation (right). The SGS terms are non-dimensionalized by $|\langle \epsilon \rangle|/\sqrt{\langle u_i u_i/2 \rangle}$.

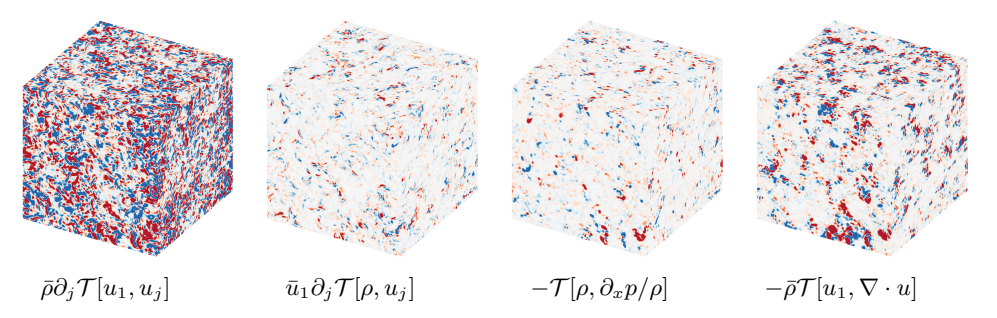


FIGURE 8. Case 2b: snapshots of fields corresponding to SGS terms in $\partial_t \bar{\rho} \bar{u}_1$ equation at $t/t_{\rm eddy} = 3$. Legend is same as figure 7.

$$\frac{\partial \bar{\rho} \bar{u}_{i}}{\partial t} + \frac{\partial}{\partial x_{j}} \left(\bar{\rho} \bar{u}_{i} \bar{u}_{i} + \bar{p} \delta_{ij} \right) + \bar{u}_{i} \frac{\partial \mathcal{T} \left[\rho, u_{j} \right]}{\partial x_{j}} + \bar{\rho} \frac{\partial \mathcal{T} \left[u_{i}, u_{j} \right]}{\partial x_{j}} - \bar{\rho} \mathcal{T} \left[u_{i}, \frac{\partial u_{j}}{\partial x_{j}} \right] - \mathcal{T} \left[\rho, \frac{1}{\rho} \frac{\partial p}{\partial x_{i}} \right] = \bar{\sigma}_{\rho u_{i}}$$

$$(4.2)$$

The SGS terms arising from viscous transport, including $\mathcal{T}\left[\rho,\sigma_{\rho u_i}/\rho\right]$ are not considered in this analysis. Snapshots of the x-component of the Case 2b SGS vector field are shown in figures 7 and 8 for the $\partial_t \bar{\rho} \tilde{u}_i$ and $\partial_t \bar{\rho} \bar{u}_i$ equations, respectively. All SGS terms are plotted on the same scale and colormap. We see that the specific stress $\mathcal{T}\left[u_i,u_j\right]$ terms in both equations are large and space-filling. While the variable-density SGS terms in both forms of the momentum equations are sparsely active, they can be large in specific regions. In particular, we note that the SGS mass flux term in the $\partial_t \bar{\rho} \tilde{u}_i$ equation is extremely small and that SGS velocity-dilatation term is the most active variable-density SGS term in the $\partial_t \bar{\rho} \bar{u}_i$ equation.

The relative importance of the variable-density SGS terms is evaluated by normalizing by the local constant-density term. The resulting ratio fields quantify the importance of the variable-density SGS terms. Since the SGS terms are vectors, the ratio of scalar projections are evaluated; two scalars are considered for this purpose. The first scalar is the magnitude of the SGS vector. If we denote a particular variable-density SGS term by T_i , and the constant-density term by T_i^{cd} , the quantity $|T_i|/|T_i^{\text{cd}}|$ indicates the relative magnitude. However, there are regions in the flow where $|T_i^{\rm cd}|$ can approach zero, which corrupts the statistics. To avoid this issue, we evaluate the regularized ratio $|T_i|/(|T_i^{\text{cd}}| + |V_i|)$, where $V_i = \bar{\sigma}_{\rho u_i}$ is the resolved-scale viscous diffusion vector and represents a physical and dimensional regularization. Thus, $|V_i|$ ensures that the statistical information derived from the ratio field, particularly the pdf tail is not arbitrary. In comparison to the SGS terms T_i , the $|V_i|$ values are typically very small. However, the V_i field is space-filling and non-zero due to the presence of non-zero strainrate in the entire domain. In the limit when $k_c \eta >> 1$ and the SGS terms are zero $(T_i, T_i^{\mathrm{cd}} \rightarrow 0)$, then $V_i \rightarrow \sigma_{\rho u_i}$ where $\sigma_{\rho u_i}$ is the viscous term in the momentum equation. Note that the SGS vectors require derivatives. Like the filters, we compute these derivatives in Fourier space.

Besides the magnitude of these terms, a scalar incorporating the orientation of the SGS vectors is also required. In this context, projection on the resolved-scale velocity vector is considered. This is a physically meaningful projection and quantifies the contribution of SGS terms to the kinetic energy associated with the resolved-scale velocity. The rate of change of the kinetic energy is

$$\frac{\partial \frac{1}{2}\bar{\rho}\tilde{u}_{i}\tilde{u}_{i}}{\partial t} = \tilde{u}_{i}\frac{\partial\bar{\rho}\tilde{u}_{i}}{\partial t} - \frac{1}{2}\tilde{u}_{i}\tilde{u}_{i}\frac{\partial\bar{\rho}}{\partial t}, \qquad \frac{\partial \frac{1}{2}\bar{\rho}\bar{u}_{i}\bar{u}_{i}}{\partial t} = \bar{u}_{i}\frac{\partial\bar{\rho}\bar{u}_{i}}{\partial t} - \frac{1}{2}\bar{u}_{i}\bar{u}_{i}\frac{\partial\bar{\rho}}{\partial t}$$
(4.3)

We see that the projection of the resolved-scale momentum equation SGS terms on the resolved-scale velocities is their contribution to the computable kinetic energy. The term $\bar{u}_i S_\rho$ appearing in $\partial_t \bar{\rho} \bar{u}_i$ is an exception; its contribution reverses sign due to the term $\partial_t \bar{\rho}$. Similar to the magnitude ratio, the ratio of the projection on resolved-scale velocity is computed with V_i to regularize the denominator. The ratio signifies the relative contribution to the resolved-scale kinetic energy.

By computing the ratio at each point in the instantaneous flow field, we can compute the probability distribution functions for these fields. A typical ratio field and its pdf are shown in figure 9. These distributions are plotted for \tilde{u}_i (figure 10) and \bar{u}_i (figure 11). Plots on the left are the magnitude ratio distributions, and those on the right are the resolved-scale velocity projection ratios. Each plot has three curves with distributions from Cases 1, 2a and 2b. Let us consider figure 10. The plots in the top row correspond to the trivariate moment term $\partial_j \mathcal{T}[\rho, u_i, u_j]$ and those in the bottom row correspond to the SGS mass flux term $-\partial_j (\mathcal{T}[\rho, u_i] \mathcal{T}[\rho, u_j]/\bar{\rho})$.

Reynolds-filtered momentum equation $\partial_t \bar{\rho} \bar{u}_i$ pdfs are plotted in figure 11 for the SGS mass flux term $\bar{u}_i \partial_j \mathcal{T}[\rho, u_j]$ (top row), SGS pressure-gradient acceleration term

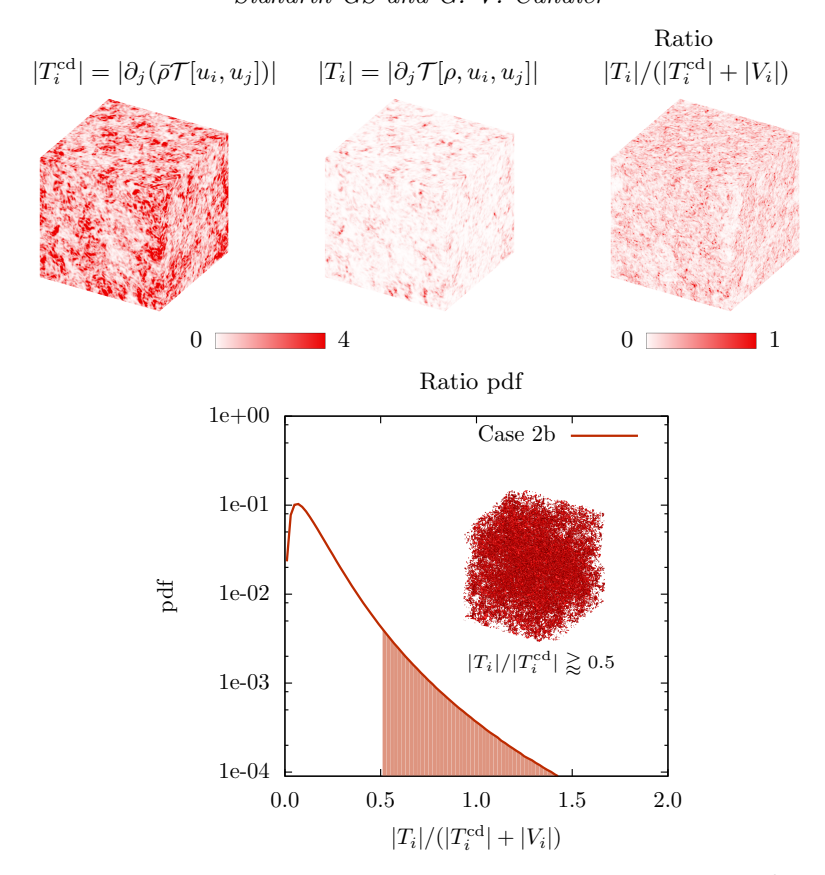


FIGURE 9. Case 2b: ratio pdf computed for trivariate moment magnitude in the $\partial_t \bar{\rho} \tilde{u}_i$ equation. The SGS terms are non-dimensionalized by $|\langle \epsilon \rangle|/\sqrt{\langle u_i u_i/2 \rangle}$. Inset picture is an isosurface enclosing regions where ratio is greater than 0.5.

 $-\mathcal{T}[\rho, \partial_i p/\rho]$ (middle row), and SGS velocity-dilatation $\bar{\rho}\mathcal{T}[u_i, \partial_j u_j]$ (bottom row). All three variable-density SGS terms are found to be non-negligible for Cases 2a and 2b, but insignificant for Case 1. For both resolved-scale momentum variables, the terms are found to be more important by means of the velocity projection ratio metric.

Integral values for the ratios are also evaluated. Average ratio values are large for Case 2b and small for Case 1. For example, the value corresponding to the trivariate term in the Favre-filtered equation by the projection metric is 0.18 for Case 2b and 0.01 for Case 1. We note that averaging the ratio field over the entire volume suppresses the importance of variable-density SGS terms as it causes the average to be biased by homogenized flow pockets where the ratio values are close to zero. Therefore, for Case 2b, we present the conditionally averaged ratio in figure 12. The conditional average is the average over regions where $|\nabla \bar{\rho}|$ is greater than a specified value $|\nabla \bar{\rho}|_c$. As the value of $|\nabla \bar{\rho}|_c$ is increased, the conditional mean of the ratios corresponding to all terms increases. This implies that when regions with strong density gradients are sampled, variable-density SGS terms become relatively more important, even in a statistical sense. For Case 2b, the mean values of the variable-density terms are found to be larger than the specific stress term using the projection metric in regions of strong resolved-scale density gradients.

Ratio distributions for the filtered vorticity transport equation (2.28) are also com-

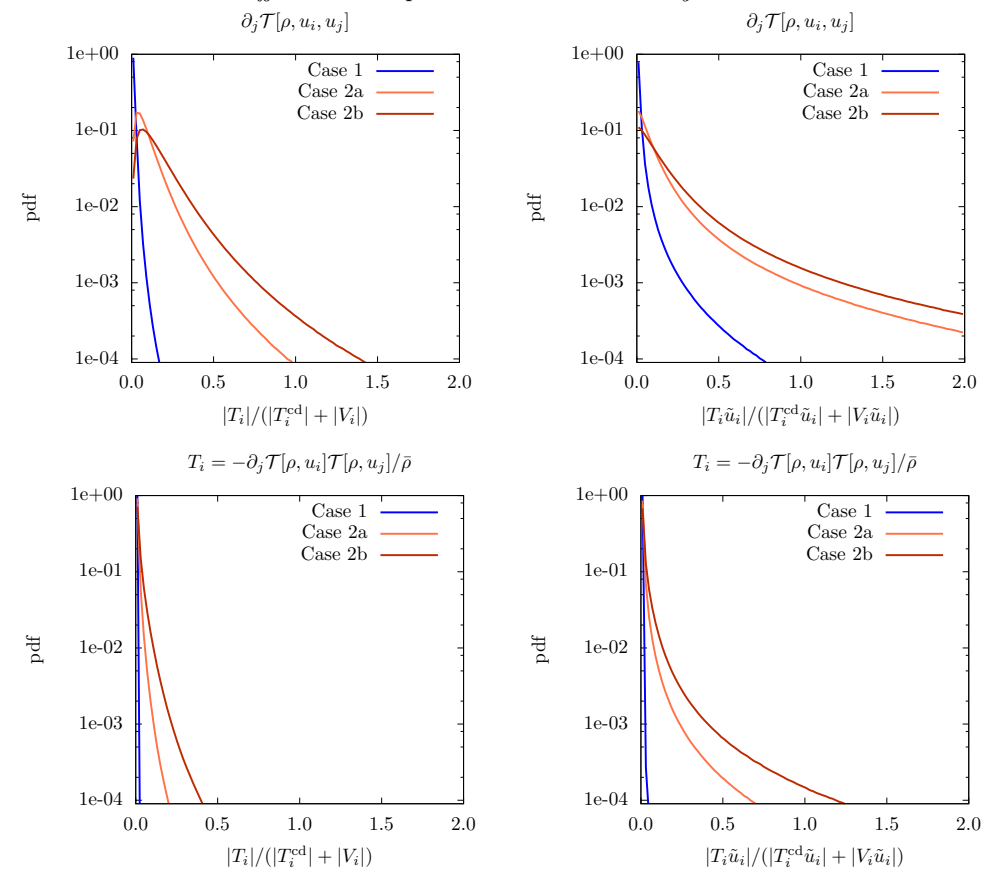


FIGURE 10. Probability distribution functions of the relative magnitude (left) and relative projection (right) for SGS terms in $\partial_t \bar{\rho} \tilde{u}_i$ equation from instantaneous flow field.

puted. There are three inviscid SGS terms in the equation: the SGS vorticity flux $\partial_j \mathcal{T}[\omega_i, u_j]$, the SGS vortex stretching term $\mathcal{T}[\omega_j, \partial_j u_i]$, and the SGS baroclinic torque $\nabla \times \mathcal{T}[\partial_i p, 1/\rho]$. The pdf plots quantifying the importance of the SGS baroclinic torque relative to the SGS vorticity flux $\partial_j \mathcal{T}[\omega_i, u_j]$ and the SGS vortex stretching term $\mathcal{T}[\omega_j, \partial_j u_i]$ are plotted in figure 13. Both metrics, magnitude, and projection on $\bar{\omega}_i$ are considered. Projecting the SGS vectors onto the resolved-scale vorticity, similar to the projection of the SGS terms in the momentum equation on the resolved-scale velocity, represents the contribution of each SGS term to the resolved-scale enstrophy $\bar{\omega}_i \bar{\omega}_i/2$. The resolved-scale viscous term $\nabla \times \bar{\sigma}_{\rho u_i}/\bar{\rho}$ is used for regularization of the denominator to compute the ratio fields. The ratio of SGS baroclinic torque to both SGS vorticity flux as well as SGS vortex stretching is computed, and is found to be important for Cases 2a and 2b, but unimportant for Case 1.

We now synthesize the important findings from the analysis. Turbulent flow fields with active variable-density effects have been investigated to quantify the role of variable-density SGS terms on the dynamics of the Favre-filtered and Reynolds-filtered velocity fields. Evidence for the significance of these terms is provided in the form of pdfs of their magnitude relative to the constant-density SGS terms. Two scalar metrics are chosen to compare the SGS vectors, namely their magnitude and their contribution to kinetic energy production and dissipation.

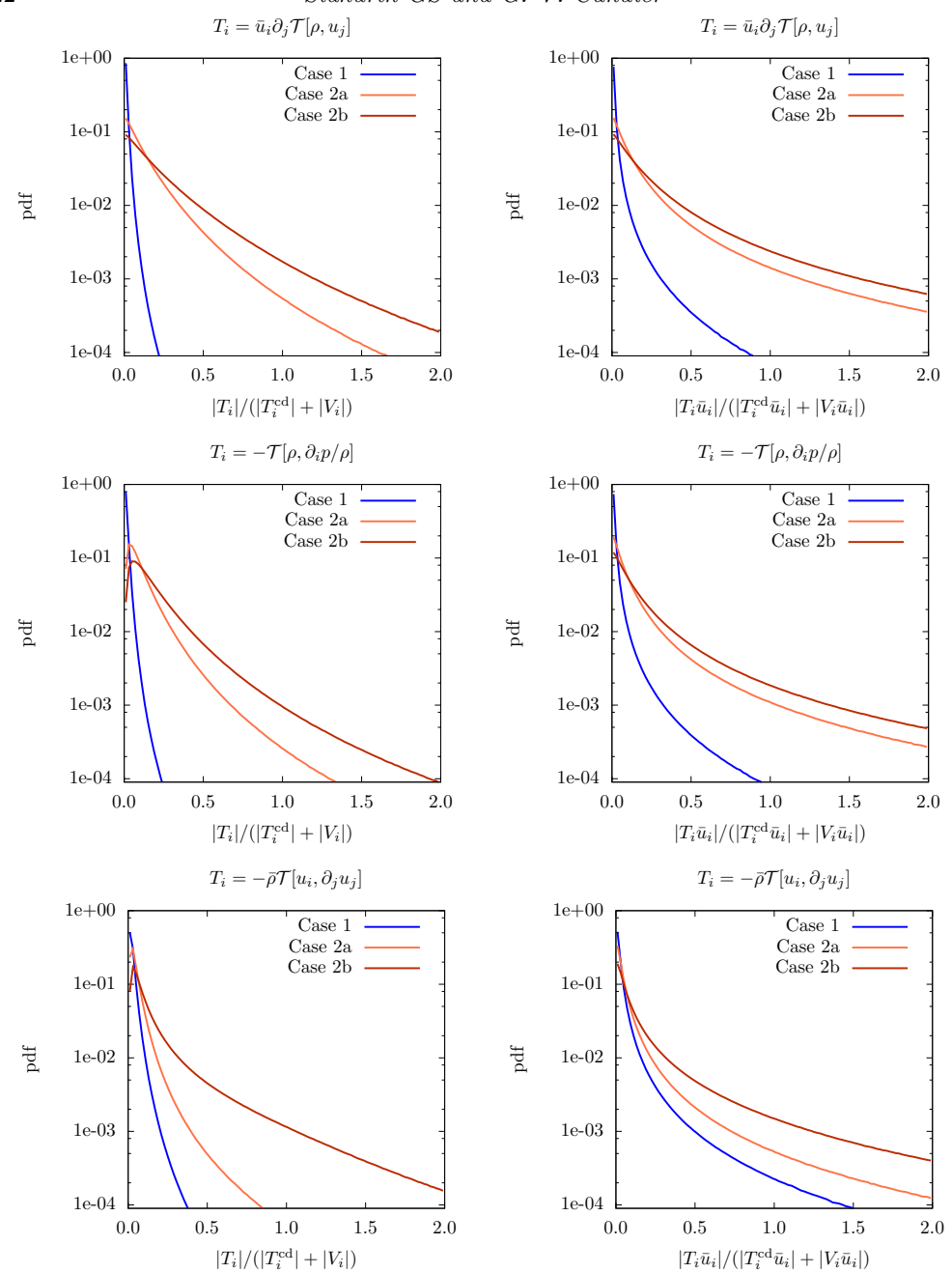


FIGURE 11. Probability distribution functions of the relative magnitude (left) and relative projection (right) for SGS terms in $\partial_t \bar{\rho} \bar{u}_i$ equation from instantaneous flow field.

For the $M_t = 0.3$ flows studied, it is found that density fluctuations arising out of compressibility alone are weak, and that SGS terms arising from small-scale density fluctuations are also negligible. However, when density fluctuations are associated with thermal inhomogeneities, they interact with the pressure gradient field to produce acceleration fluctuations, thereby affecting velocity gradients. Not only is vorticity affected, but the dilatation content is also significantly altered. Therefore, flow compressibility

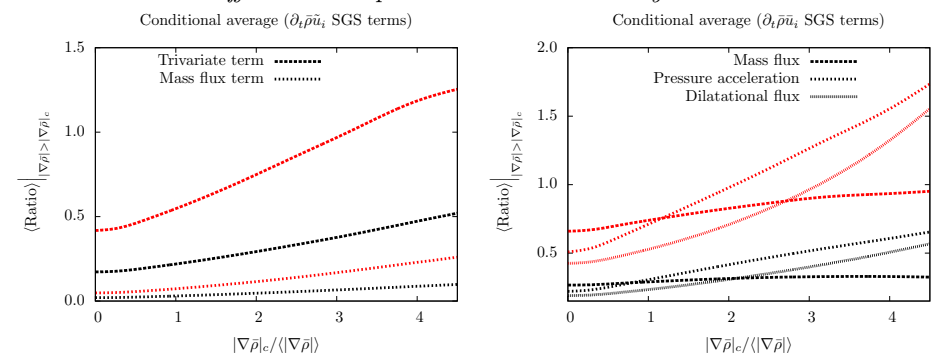


FIGURE 12. Conditional volumetric averages of relative magnitude (black) and relative projection (red) for SGS terms in Favre-filtered equation (left) and Reynolds-filtered equation (right) from instantaneous flow field.

strongly couples with thermal density inhomogeneities, and consequently, the dynamics of compressible variable-density turbulence are inherently different from incompressible variable-density turbulence (Sandoval 1995). Although we do not study compressible turbulent mixing of variable-density fluids with different molecular weights, such flows are expected to exhibit non-negligible variable-density SGS effects as well.

The analysis discusses variable-density effects on the Favre-filtered velocity SGS stress tensor in terms of central moments under the filter, which represent the spatial correlation between small scales. The trivariate moment $\mathcal{T}[\rho, u_i, u_j]$ is found to be the most dynamically important variable-density term in the SGS stress. The physics of this term merit attention because it contributes significantly to the computable resolved-scale kinetic energy $\bar{\rho}\tilde{u}_i\tilde{u}_i/2$.

We also present an alternate form of the Reynolds-filtered Navier-Stokes equations. The equations are novel because they do not involve time derivatives of unclosed terms and all unclosed terms involve only second moments under the filter operator. Using the new Reynolds-filtered momentum equation, we isolate the SGS inertial and dilatational effects and establish the dynamical importance of specific terms. The new Reynolds-filtered equations represent the effect of SGS pressure-acceleration, as well as the SGS mass flux and SGS dilatation correlations in resolved-scale mass, velocity, and internal energy.

From the point of view of large eddy simulations, the analysis has implications on the modeling variable-density SGS effects. The new SGS terms provide a framework to study variable-density counter-gradient diffusion independently of the constant-density SGS terms. For example, in Case 2b, we find that the SGS mass flux and SGS pressure-acceleration terms have a net positive contribution to $(1/2)\partial_t \bar{\rho} \bar{u}_i \bar{u}_i$, as opposed to the SGS specific stress, which has a net negative contribution. In other words, while the constant-density SGS term drains energy from the large scales in the mean sense, these two variable-density SGS terms transfer kinetic energy to the large scales. Counter-gradient diffusion is particularly important for turbulent combustion in which dilatation (Veynante et al. 1997; Yoshizawa et al. 2009; O'Brien et al. 2014) and pressure gradients (Veynante & Poinsot 1997) correlate with counter-gradient diffusion of species and kinetic energy. Future work will involve developing and testing subgrid-scale closures for the variable-density SGS terms in Favre and Reynolds-filtered formulations in different classes of flows.

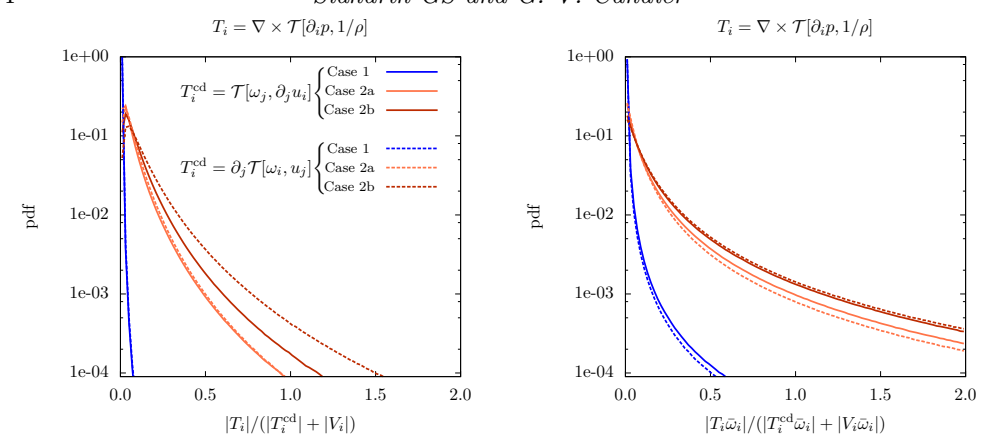


FIGURE 13. Probability distribution function of relative magnitude (left) and relative projection (right) for SGS terms in $\partial_t \bar{\omega}_i$ equation from instantaneous flow-field.

5. Conclusions

This paper identifies the role of subgrid-scale density fluctuations on resolved-scale velocity, using both density-weighted and non-density-weighted forms of the governing equations. We first discuss the filtered Navier-Stokes equations in the conventional Favre-filtered framework and follow with a novel derivation of the Reynolds-filtered form of the equations. The filtered velocity dynamics are studied because the curl of the filtered velocity is the filtered vorticity. Important variable-density effects such as the SGS baroclinic torque appear in the transport equation of filtered vorticity. On the other hand, the curl of the Favre-filtered velocity follows different dynamics and can differ significantly from the filtered vorticity, particularly when small-scale density fluctuations are strong.

The conventional resolved-scale momentum equation derived without density weighting contains the time derivative of the subgrid-scale mass flux. This unsteady SGS term makes the equation cumbersome from a modeling perspective. Therefore, we derive a new set of Reynolds-filtered equations for mass, momentum, and energy by decoupling the transport of SGS mass flux and SGS kinetic energy from the equations. In addition to having only spatial SGS terms, the new Reynolds-filtered equations involve only double correlations of the flow state.

In the equations for the resolved-scale momentum, we represent the SGS terms by expressing them as central moments under the filter operator. Using this method, we isolate the terms that involve the density or dilatation field, and the SGS terms containing only the specific stress $\overline{u_iu_j} - \overline{u}_i\overline{u}_j$ appear explicitly. We refer to such terms as constant-density SGS terms because they are the only active terms in a constant-density turbulent flow. After partitioning the SGS terms into variable-density and constant-density terms, it is natural to compare their relative strength. For this purpose, we carry out direct numerical simulations of two types of compressible decaying turbulence. In the first case, density fluctuations are primarily barotropic and arise from the compressibility of the flow, which is set to a moderate value. The other case involves the mixing of thermally inhomogeneous variable-density fluid regions with identical flow parameters. Therefore, the main content of the density fluctuations is entropic. It is found that the variable-density SGS terms are negligible in the first case, but important in the second. This is attributed to the presence of strong inertial effects on small-scale turbulent flow features in the latter case.

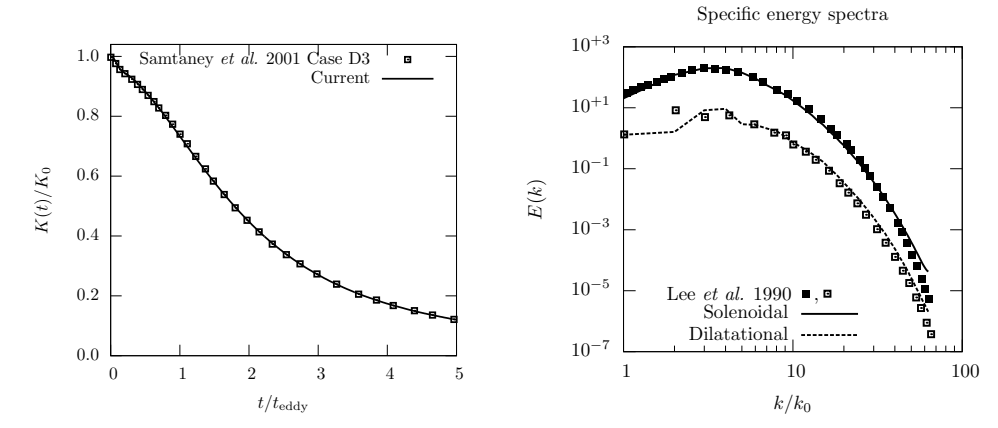


FIGURE 14. Comparison of decaying isotropic compressible turbulence simulations with literature.

We conclude that the effects of small-scale density variations on the dynamics of large-scale velocity and vorticity can be important in compressible flows involving the mixing of variable-density fluids. In the Favre-filtered momentum equation, these effects are embedded in the trivariate moment term (triple correlation). Whereas, in the Reynolds-filtered momentum equation, these effects appear separately as the SGS pressure-gradient acceleration, SGS velocity dilatation, and SGS mass flux convection. Understanding and quantifying the role played by these terms under different flow conditions will pave the way to the design of improved closures for variable-density turbulence.

We thank Dr. Pramod Subbareddy and the reviewers for suggestions that improved the manuscript. This work was sponsored by Air Force Office of Scientific Research under grant numbers FA9550-12-1-0461, FA9550-17-1-0250 and Department of Energy/National Nuclear Security Administration Award number DE-NA0002382. The views and conclusions contained herein are those of the authors and should not be interpreted as necessarily representing the official policies or endorsements, either expressed or implied, of the funding agencies or the U.S. Government.

6. Appendix

The sensitivity of the analysis to the choice of simulation and filtering parameters is briefly discussed in this section. A comparison of kinetic energy decay and instantaneous radial spectra with simulations reported in literature is shown in figure 14. The effect of grid resolution on Case 2b flow-field at a fixed time $t/t_{\rm eddy}=3.0$ is shown in figure 15. The spectral content and the intermittency of the instantaneous flow-field are properly captured with a grid resolution of 512^3 . To quantify the sensitivity of the relative importance of the subgrid-scale variable density terms, we focus on the resolved-scale momentum equation corresponding to the filtered velocity \bar{u}_i . The effect of filter type, cutoff wavenumber for the exponential filter, initial and instantaneous length-scale Reynolds number and the randomness of the initial density distribution is considered. The results are displayed in figures 16-19. The relative importance of the variable-density SGS terms is found to be insensitive to all the parameters mentioned above, making the conclusions drawn in this paper general for decaying compressible variable-density turbulence.

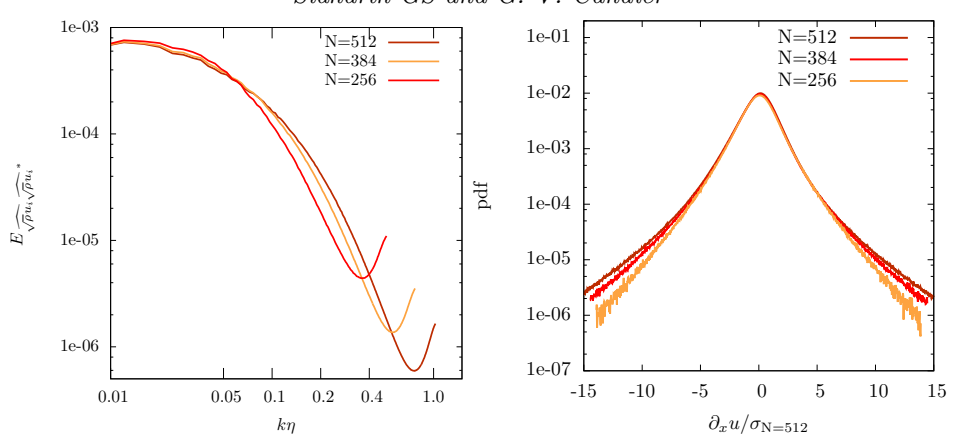


Figure 15. Grid refinement study of the field statistics at $t/t_{\rm eddy} = 3$ for Case 2b

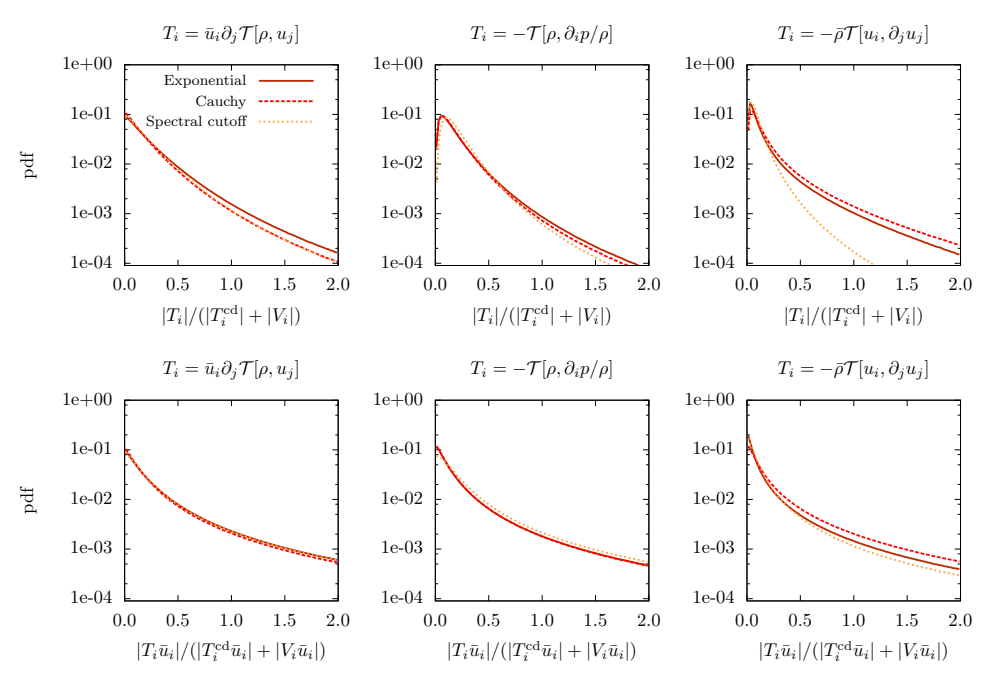


FIGURE 16. Effect of filter type on relative strength of variable-density SGS terms in $\bar{\rho}\bar{u}_i$ equation (Case 2b).

REFERENCES

ADUMITROAIE, V., RISTORCELLI, J. R. & TAULBEE, D. B. 1999 Progress in Favre-Reynolds stress closures for compressible flows. *Physics of Fluids* 11 (9), 2696–2719.

BAKOSI, J. & RISTORCELLI, J. 2011 Extending the langevin model to variable-density pressure-gradient-driven turbulence. *Journal of Turbulence* 12.

Banerjee, A., Gore, R. A. & Andrews, M. J. 2010 Development and validation of a turbulent-mix model for variable-density and compressible flows. *Physical Review E* 82 (4), 046309.

BILGER, R. 1976 Turbulent jet diffusion flames. *Progress in Energy and Combustion Science* 1 (2-3), 87–109.

Boersma, B. J. & Lele, S. K. 1999 Large eddy simulation of compressible turbulent jets. Center for Turbulence Research Annual Research Briefs pp. 365–377.

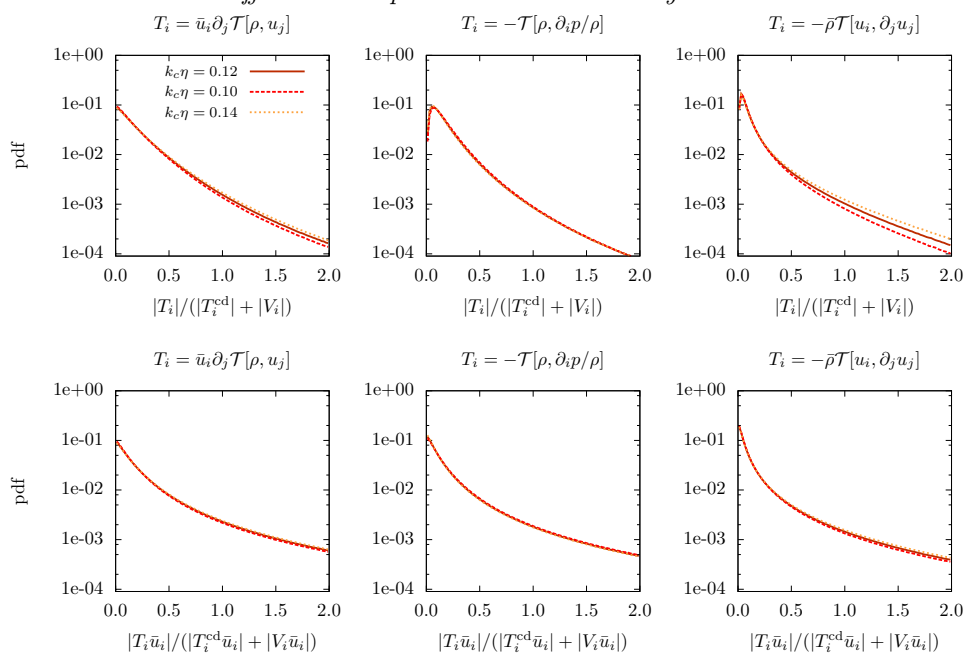


FIGURE 17. Effect of cutoff wavenumber used in the exponential filter on relative strength of variable-density SGS terms in $\bar{\rho}\bar{u}_i$ equation (Case 2b).

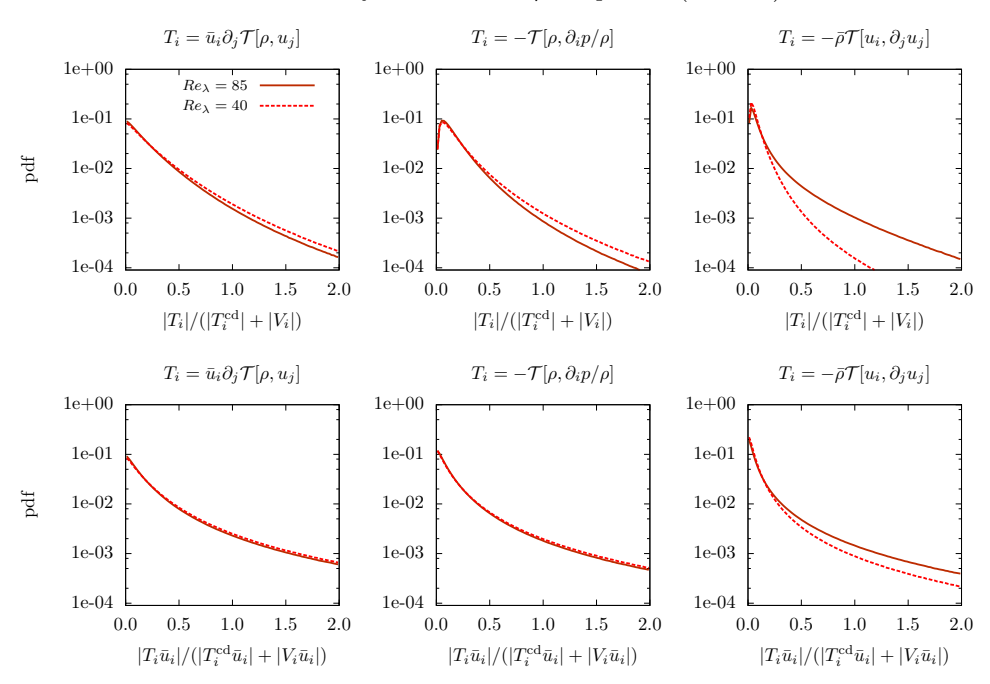


FIGURE 18. Effect of Reynolds number on relative strength of variable-density SGS terms in $\bar{\rho}\bar{u}_i$ equation. The Taylor scale Reynolds number shown in the plots corresponds to the instantaneous flow-field (Case 2b).

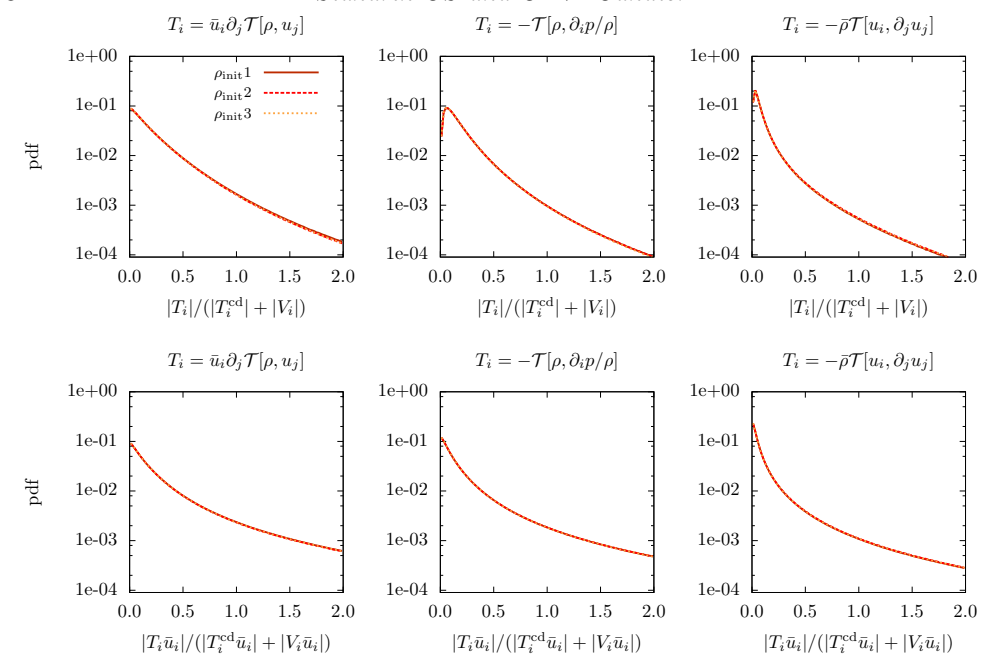


FIGURE 19. Effect of the randomness of the initial density field distribution on relative strength of variable-density SGS terms in $\bar{\rho}\bar{u}_i$ equation (Case 2b).

Bray, K., Libby, P. A., Masuya, G. & Moss, J. 1981 Turbulence production in premixed turbulent flames. *Combustion Science and Technology* **25**.

Brenner, H. 2009 Bi-velocity hydrodynamics. *Physica A: Statistical Mechanics and its Applications* **388** (17), 3391–3398.

BROUILLETTE, M. 2002 The Richtmyer-Meshkov instability. *Annual Review of Fluid Mechanics* **34** (1), 445–468.

Brown, G. L. & Roshko, A. 1974 On density effects and large structure in turbulent mixing layers. *Journal of Fluid Mechanics* **64** (4), 775–816.

Candler, G. V., Subbareddy, P. K. & Brock, J. M. 2015 Advances in computational fluid dynamics methods for hypersonic flows. $Journal\ of\ Spacecraft\ and\ Rockets$.

Chakraborty, N., Wang, L., Konstantinou, I. & Klein, M. 2017 Vorticity statistics based on velocity and density-weighted velocity in premixed reactive turbulence. *Journal of Turbulence* 18 (9), 825–853.

Chassaing, P. 1997 Some problems on single point modeling of turbulent, low-speed, variable density fluid motions. In *IUTAM Symposium on Variable Density Low-Speed Turbulent Flows*, pp. 65–84. Springer.

Chassaing, P. 2001 The modeling of variable density turbulent flows. a review of first-order closure schemes. Flow, turbulence and combustion 66 (4), 293–332.

Chassaing, P., Antonia, R., Anselmet, F., Joly, L. & Sarkar, S. 2013 Variable density fluid turbulence. Springer Science & Business Media.

Chassaing, P., Harran, G. & Joly, L. 1994 Density fluctuation correlations in free turbulent binary mixing. *Journal of Fluid Mechanics* 279, 239–278.

Chesnel, J., Reveillon, J., Menard, T. & Demoulin, F.-X. 2011 Large eddy simulation of liquid jet atomization. *Atomization and Sprays* 21 (9).

Chomiak, J. & Nisbet, J. 1995 Modeling variable density effects in turbulent flames: some basic considerations. *Combustion and flame* **102** (3), 371–386.

Donzis, D. A., Sreenivasan, K. & Yeung, P. 2010 The batchelor spectrum for mixing of passive scalars in isotropic turbulence. Flow, turbulence and combustion 85 (3), 549–566.

Favre, A. 1969 Statistical equations of turbulent gases. *Problems of hydrodynamics and continuum mechanics* pp. 231–266.

- FAVRE, A. J. 1992 Formulation of the statistical equations of turbulent flows with variable density. In *Studies in Turbulence*, pp. 324–341. Springer.
- Ferrer, P. J. M., Lehnasch, G. & Mura, A. 2017 Compressibility and heat release effects in high-speed reactive mixing layers i.: Growth rates and turbulence characteristics. *Combustion and Flame* **180**, 284–303.
- Fontane, J. & Joly, L. 2008 The stability of the variable-density Kelvin-Helmholtz billow. Journal of Fluid Mechanics 612, 237–260.
- FREUND, J. B., LELE, S. K. & MOIN, P. 2000 Compressibility effects in a turbulent annular mixing layer. part 1. turbulence and growth rate. *Journal of Fluid Mechanics* **421**, 229–267
- FRIELER, C. & DIMOTAKIS, P. 1988 Mixing and reaction at low heat release in the non-homogeneous shear layer. First National Fluid Dynamics Congress .
- GERMANO, M. 1992 Turbulence: the filtering approach. *Journal of Fluid Mechanics* **238**, 325–336
- GERMANO, M. 1996 Averaging procedures for the large eddy simulation of variable density flows.

 IUTAM Symposium on Variable Density Low-Speed Turbulent Flows pp. 101–108.
- GERMANO, M., ABB, A., ARINA, R. & BONAVENTURA, L. 2014 On the extension of the eddy viscosity model to compressible flows. *Physics of Fluids* **26** (4).
- GETSINGER, D. R., HENDRICKSON, C. & KARAGOZIAN, A. R. 2012 Shear layer instabilities in low-density transverse jets. *Experiments in fluids* **53** (3), 783–801.
- GILL, A., GREEN, J. & SIMMONS, A. 1974 Energy partition in the large-scale ocean circulation and the production of mid-ocean eddies. In *Deep Sea Research and Oceanographic Abstracts*, vol. 21, pp. 499IN1509–508528. Elsevier.
- GOTTLIEB, S., Shu, C.-W. & Tadmor, E. 2001 Strong stability-preserving high-order time discretization methods. SIAM review 43 (1), 89–112.
- GRIGORIEV, I. A., WALLIN, S., BRETHOUWER, G. & JOHANSSON, A. V. 2015 Capturing turbulent density flux effects in variable density flow by an explicit algebraic model. *Physics of Fluids* **27** (4), 045108.
- Hamba, F. 1999 Effects of pressure fluctuations on turbulence growth in compressible homogeneous shear flow. *Physics of Fluids* **11** (6), 1623–1635.
- JOLY, L., FONTANE, J. & CHASSAING, P. 2005 The Rayleigh-Taylor instability of twodimensional high-density vortices. *Journal of Fluid Mechanics* 537, 415–431.
- Klein, M., Kasten, C., Gao, Y. & Chakraborty, N. 2015 A-priori direct numerical simulation assessment of sub-grid scale stress tensor closures for turbulent premixed combustion. *Computers & Fluids* 122, 1–11.
- KOVASZNAY, L. S. 1953 Turbulence in supersonic flow. *Journal of the Aeronautical Sciences* **20** (10).
- Kreuzinger, J., Friedrich, R. & Gatski, T. B. 2006 Compressibility effects in the solenoidal dissipation rate equation: A priori assessment and modeling. *International Journal of Heat and Fluid Flow* **27** (4), 696 706.
- Lagha, M., Kim, J., Eldredge, J. & Zhong, X. 2011 A numerical study of compressible turbulent boundary layers. *Physics of fluids* **23** (1), 015106.
- LARUE, J. C. & LIBBY, P. A. 1977 Measurements in the turbulent boundary layer with slot injection of helium. *The Physics of Fluids* **20** (2), 192–202.
- Lele, S. K. 1994 Compressibility effects on turbulence. Annual review of fluid mechanics ${\bf 26}$ (1), 211-254.
- LIBBY, P. A. & BRAY, K. 1977 Variable density effects in premixed turbulent flames. AIAA J ${\bf 15}$ (8), 1186–1193.
- Libby, P. A. & Bray, K. 1981 Countergradient diffusion in premixed turbulent flames. AIAA Journal 19 (2).
- LINDSTEDT, R. & VAOS, E. 1999 Modeling of premixed turbulent flames with second moment methods. *Combustion and Flame* **116** (4), 461–485.
- LIPATNIKOV, A. & CHOMIAK, J. 2010 Effects of premixed flames on turbulence and turbulent scalar transport. *Progress in Energy and Combustion Science* **36** (1), 1–102.
- LIVESCU, D. & RISTORCELLI, J. 2007 Buoyancy-driven variable-density turbulence. *Journal of Fluid Mechanics* **591**, 43–71.

- MACCORMACK, R. W. 2014 Numerical computation of compressible and viscous flow. American Institute of Aeronautics and Astronautics.
- MILLER, M., BOWMAN, C. & MUNGAL, M. 1998 An experimental investigation of the effects of compressibility on a turbulent reacting mixing layer. *Journal of Fluid Mechanics* **356**, 25–64.
- MONKEWITZ, P. A., BECHERT, D. W., BARSIKOW, B. & LEHMANN, B. 1990 Self-excited oscillations and mixing in a heated round jet. *Journal of Fluid Mechanics* 213, 611–639.
- O'BRIEN, J., URZAY, J., IHME, M., MOIN, P. & SAGHAFIAN, A. 2014 Subgrid-scale backscatter in reacting and inert supersonic hydrogen-air turbulent mixing layers. *Journal of Fluid Mechanics* **743**, 554–584.
- Pantano, C. & Sarkar, S. 2002 A study of compressibility effects in the high-speed turbulent shear layer using direct simulation. *Journal of Fluid Mechanics* **451**, 329–371.
- Patel, A., Boersma, B. J. & Pecnik, R. 2016 The influence of near-wall density and viscosity gradients on turbulence in channel flows. *Journal of Fluid Mechanics* 809, 793–820.
- Pierrehumbert, R. & Swanson, K. 1995 Baroclinic instability. Annual review of fluid mechanics 27 (1), 419–467.
- RANJAN, D., OAKLEY, J. & BONAZZA, R. 2011 Shock-bubble interactions. *Annual Review of Fluid Mechanics* 43, 117–140.
- REINAUD, J., JOLY, L. & CHASSAING, P. 2000 The baroclinic secondary instability of the two-dimensional shear layer. *Physics of Fluids* **12** (10), 2489–2505.
- RISTORCELLI, J. 1993 A representation for the turbulent mass flux contribution to reynoldsstress and two-equation closures for compressible turbulence. *ICASE Report* (93-88).
- RISTORCELLI, J. R. & BLAISDELL, G. A. 1997 Consistent initial conditions for the dns of compressible turbulence. *Physics of Fluids* **9** (1), 4–6.
- ROBIN, V., MURA, A. & CHAMPION, M. 2011 Direct and indirect thermal expansion effects in turbulent premixed flames. *Journal of Fluid Mechanics* **689**, 149–182.
- Rubinstein, R. & Erlebacher, G. 1997 Transport coefficients in weakly compressible turbulence. *Physics of Fluids* **9** (10), 3037–3057.
- Sabelnikov, V. A. & Lipatnikov, A. N. 2017 Recent advances in understanding of thermal expansion effects in premixed turbulent flames. *Annual Review of Fluid Mechanics* 49, 91–117.
- Samtaney, R., Pullin, D. I. & Kosović, B. 2001 Direct numerical simulation of decaying compressible turbulence and shocklet statistics. *Physics of Fluids* **13** (5), 1415–1430.
- SANDOVAL, D. L. 1995 The dynamics of variable-density turbulence. PhD thesis.
- SARKAR, S. 1992 The pressure–dilatation correlation in compressible flows. *Physics of Fluids A: Fluid Dynamics* 4 (12), 2674–2682.
- Schumacher, J., Scheel, J. D., Krasnov, D., Donzis, D. A., Yakhot, V. & Sreenivasan, K. R. 2014 Small-scale universality in fluid turbulence. *Proceedings of the National Academy of Sciences* 111 (30), 10961–10965.
- Schwarzkopf, J. D., Livescu, D., Gore, R. A., Rauenzahn, R. M. & Ristorcelli, J. R. 2011 Application of a second-moment closure model to mixing processes involving multicomponent miscible fluids. *Journal of Turbulence* 12, N49.
- Serra, S., Robin, V., Mura, A. & Champion, M. 2014 Density variations effects in turbulent diffusion flames: modeling of unresolved fluxes. *Combustion Science and Technology* **186** (10-11), 1370–1391.
- Shih, T.-H., Lumley, J. L. & Janicka, J. 1987 Second-order modelling of a variable-density mixing layer. *Journal of Fluid Mechanics* **180**, 93–116.
- SIDHARTH, G., CANDLER, G. V. & DIMOTAKIS, P. E. 2014 Baroclinic torque and implications for subgrid-scale modeling. 7th AIAA Theoretical Fluid Mechanics Conference .
- Sinha, K. & Candler, G. V. 2003 Turbulent dissipation-rate equation for compressible flows. AIAA Journal 41 (6), 1017–1021.
- SPINA, E. F., SMITS, A. J. & ROBINSON, S. K. 1994 The physics of supersonic turbulent boundary layers. *Annual Review of Fluid Mechanics* **26** (1), 287–319.
- Sreenivasan, K., Raghu, S. & Kyle, D. 1989 Absolute instability in variable density round jets. *Experiments in Fluids* **7** (5), 309–317.
- Subbareddy, P. K., Bartkowicz, M. D. & Candler, G. V. 2014 Direct numerical simulation

- of high-speed transition due to an isolated roughness element. *Journal of Fluid Mechanics* **748**, 848–878.
- Subbareddy, P. K. & Candler, G. V. 2009 A fully discrete, kinetic energy consistent finite-volume scheme for compressible flows. *Journal of Computational Physics* **228** (5), 1347–1364
- Sun, X.-B. & Lu, X.-Y. 2006 A large eddy simulation approach of compressible turbulent flow without density weighting. *Physics of Fluids* **18** (11).
- Taulbee, D. & Vanosdol, J. 1991 Modeling turbulent compressible flows: the mass fluctuating velocity and squared density. AIAA paper 524, 1991.
- Thomas, G., Bambrey, R. & Brown, C. 2001 Experimental observations of flame acceleration and transition to detonation following shock-flame interaction. *Combustion Theory and Modelling* 5 (4), 573–594.
- TRETTEL, A. & LARSSON, J. 2016 Mean velocity scaling for compressible wall turbulence with heat transfer. *Physics of Fluids* **28** (2), 026102.
- VAN DRIEST, E. R. 1951 Turbulent boundary layer in compressible fluids. *Journal of the Aeronautical Sciences* 18 (3).
- VEYNANTE, D. & POINSOT, T. 1997 Effects of pressure gradients on turbulent premixed flames. Journal of Fluid Mechanics 353, 83–114.
- VEYNANTE, D., TROUVÉ, A., BRAY, K. & MANTEL, T. 1997 Gradient and counter-gradient scalar transport in turbulent premixed flames. *Journal of Fluid Mechanics* 332, 263–293.
- VREMAN, A. W. 1995 Direct and large-eddy simulation of the compressible turbulent mixing layer. University of Twente.
- VREMAN, A. W., SANDHAM, N. & Luo, K. 1996 Compressible mixing layer growth rate and turbulence characteristics. *Journal of Fluid Mechanics* **320**, 235–258.
- Yoshizawa, A. 1986 Statistical theory for compressible turbulent shear flows, with the application to subgrid modeling. *Physics of Fluids* **29** (7), 2152–2164.
- Yoshizawa, A., Fujiwara, H., Abe, H. & Matsuo, Y. 2009 Mechanisms of countergradient diffusion in turbulent combustion. *Physics of Fluids* **21** (1).
- Yoshizawa, A., Matsuo, Y. & Mizobuchi, Y. 2013 A construction of the Reynolds-averaged turbulence transport equations in a variable-density flow, based on the concept of mass-weighted fluctuations. *Physics of Fluids* **25** (7).
- Zeman, O. 1990 Dilatation dissipation: The concept and application in modeling compressible mixing layers. *Physics of Fluids A* 2 (2), 178–188.
- Zeman, O. 1991 On the decay of compressible isotropic turbulence. *Physics of Fluids A* **3** (5), 951–955.